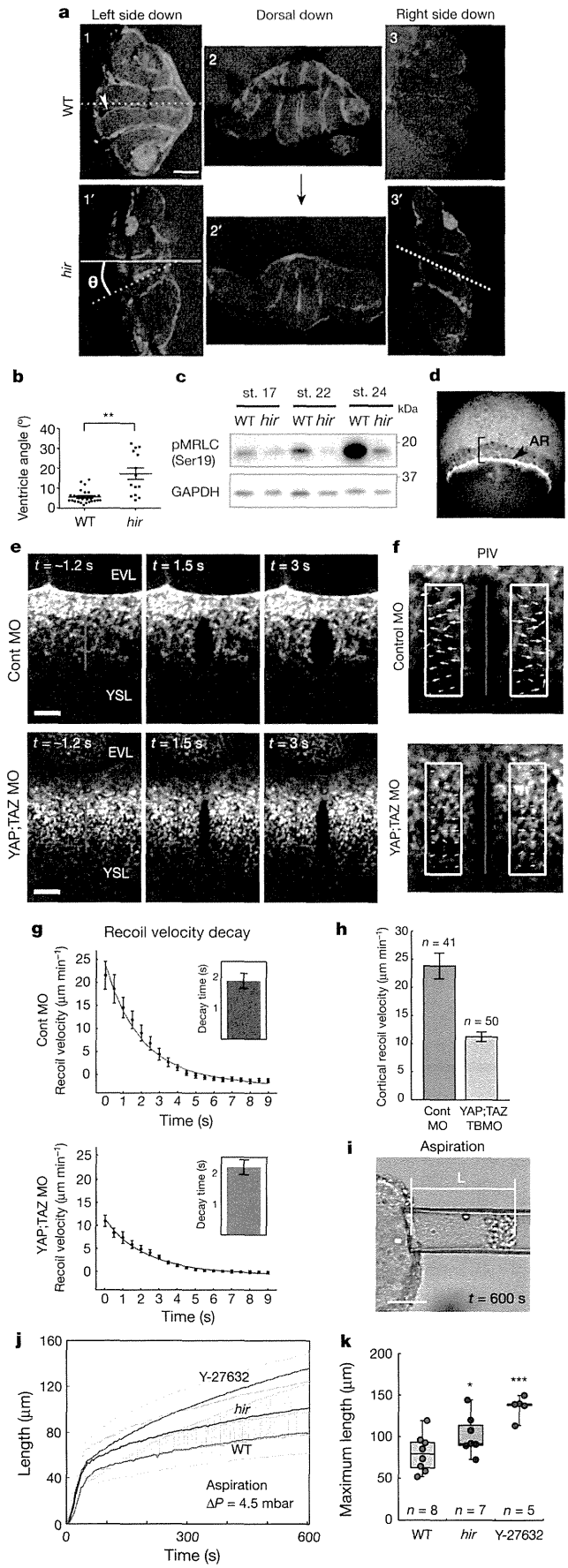

Figure 2 | Tissue tension is reduced in *hir* mutants. **a**, Embryos kept left side down (**a1**, **a1′**), dorsal facing down (**a2**, **a2′**) and right side down (**a3**, **a3′**) from st. 17–25, stained with phalloidin (green, F-actin) and TO-PRO-3 (blue, nucleus). Large black arrow, direction of gravity; θ, angle that the tangent along the brain ventricle (dotted lines in **a1**, **a1′**) makes with horizontal solid line. **b**, Range of collapse of mutant and WT embryos kept sideways. Error bars, ± s.e.m. $^{**}P < 0.01$, *t*-test (see Fig. 2 Source Data). **c**, Immunoblotting of phospho-myosin regulatory light chain (pMRLC, Ser19) and control (GAPDH) (Supplementary Fig. 1). **d**, Actomyosin-labelled *Tg(actb2:myl12.1-eGFP)* zebrafish embryos at 75% epiboly. Arrowhead, YSL actomyosin ring (AR) at the margin of the EVL. Bracket, for analysis of EVL shape anisotropy (Extended Data Fig. 3a). **e**, The actomyosin ring was cut along a 20 μm-long line (red) perpendicular to the EVL/YSL boundary in MO-injected embryos, when control MO injected embryos were at 70–80% epiboly. **f**, Particle image velocimetry (PIV) quantifies the velocity field (yellow arrows) of the recoiling actomyosin network. **g**, Averaged temporal recoil velocity curves, control MO ($n = 41$) and YAP;TAZ KD conditions ($n = 50$). Error bars, error of the mean at 95% confidence. Exponential fit function with a linear offset (black solid line) yields the characteristic decay time (inset) and **h**, the initial recoil velocity for the control MO (23.8 ± 2.3 μm min^{-1}) and YAP;TAZ KD conditions (11.2 ± 0.8 μm min^{-1}). Error bars, 95% confidence interval for the fit results. **i**, Snapshot at the end of aspiration (600 s) of st. 22 neural tube with constant pressure ($\Delta P = 4.5$ mbar). **j**, The curves of the tongue length over time to measure the aspiration of WT, *hir* mutant and ROCK inhibitor (Y27632)-treated neural tube explants. Error bars, ± s.d. Maximum tongue lengths measured at 600 s were compared by *t*-test in **k**. Box plots represent 5%, 25%, median, 75%, and 95%. $^{*}P < 0.05$, $^{***}P < 0.001$. Scale bars, 40 μm in **a**, **i**, 10 μm in **e**.

and organs including neural tube and somites gradually became flattened and improperly aligned (Fig. 1d). Lenses were misaligned outside the eyes (Fig. 1a2, a2′). Mutant lens placodes expressing *sox3* formed normally adjacent to the retina up to st. 20, but then became fragmented and detached from the retina (Fig. 1e1′, e2′, Extended Data Fig. 1a, b and Supplementary Videos 1, 2). These fragments gradually rounded up with some re-attaching to the retina to form ectopic lenses that were not incorporated (Fig. 1e). Thus, tissue flattening and misalignment defects are associated with the flattened mutant phenotype.

Positional cloning identified a nonsense mutation of Leu164 (TTG to TAG) in the WW1 domain of YAP in *hir* (Extended Data Fig. 1c, d). YAP is the nuclear executor of the Hippo pathway and regulates organ growth via stimulation of cell proliferation[7–9]. In wild-type (WT) embryos, YAP transcripts are ubiquitous throughout development[10]. Medaka maternal *YAP* messenger RNA (mRNA) was present at st. 10 in *hir* before onset of zygotic gene expression, but undetectable after st. 18 (Extended Data Fig. 1e). Morpholino oligonucleotide (MO) YAP knockdown (KD) in WT embryos recapitulated the *hir* phenotype (Extended Data Fig. 2a–c, Supplementary Tables 1, 2), and ubiquitous recombinant *YAP* mRNA expression rescued the *hir* phenotype (Extended Data Fig. 1f). In addition, perturbation of maternal *YAP* mRNA translation in *hir* mutant embryos by YAP translation-blocking (TB) MO (mYAP KD *hir* embryos) elicited a more severe blastopore closure and body flattening phenotype than in *hir* zygotic YAP mutants (Fig. 1b3, b3′, c, Supplementary Table 2). Blastopore closure defects, but not flattening, have been reported in YAP KD zebrafish and *Xenopus*[11]. Since TAZ is a functional paralogue of YAP[12], we evaluated its contribution to the YAP KD phenotype in zebrafish. YAP;TAZ double KD zebrafish embryos exhibited more pronounced blastopore closure defects than YAP KD alone (Extended Data Fig. 2d–h). YAP-4SA, which lacks four serines and predominantly localizes to the nucleus[13], rescued the *hir* phenotype more efficiently than WT YAP (Extended Data Fig. 1f), suggesting that the *hir* phenotype depends on nuclear YAP. The main nuclear function of YAP is to promote proliferation and inhibit cell death[14]. *hir* embryos had increased cell death from st. 22 to 26 after body flattening had initiated (increased cell death per se does not lead to body flattening[5,6]). Cell proliferation remained close to normal in *hir* embryos but was strongly suppressed in TAZ KD (and YAP/TAZ double KD) medaka embryos (Extended Data Fig. 2i, j). Thus, in medaka, cell

proliferation is mainly regulated by TAZ, while YAP is predominantly required for 3D body shape.

Three dpf *hir* mutants showed different orientations of body flattening. We therefore examined whether collapse correlated with the direction of gravity. Mutant embryos maintained either right-side or left-side down relative to the earth collapsed towards the earth as indicated by the ventricle tangent (Fig. 2a). Average collapse angle, θ, in mutant embryos was $17.3 \pm 10.7^{\circ}$ ($n = 14$; Fig. 2b) compared to $5.6 \pm 3.3^{\circ}$ ($n = 26, P < 0.01$) in WT. Mutant embryos maintained dorsal side down exhibited apparently uniform dorso-ventral compression (Fig. 2a2, a2′). Thus, flattening in *hir* embryos reflects an inability to withstand external forces (that is, gravity), suggesting reduced tissue tension.

Tissue tension is generated primarily by actomyosin contraction[15]. During WT organogenesis, global levels of phosphorylated myosin regulatory light chain (pMRLC), indicative of actomyosin activity, increased (Fig. 2c), while in *hir* mutants they began decreasing as the blastopore closes (st. 17, 25 hpf), and continued decreasing coincident with tissue collapse and body flattening. To assess tissue tension during blastopore closure, we analysed a surface epithelial cell layer, the enveloping layer (EVL)[16] (Extended Data Fig. 3a1). Comparison of EVL shape anisotropy between WT and *hir* embryos suggested that tissue tension in *hir* is reduced within the EVL (Extended Data Fig. 3a, b). We also quantified actomyosin network tension within the yolk syncytial layer (YSL) of zebrafish embryos with compromised YAP function expressing enhanced green fluorescent protein (EGFP)–myosin light chain protein, Tg(*actb2:myl12.1-eGFP*)[17]. The YSL actomyosin network close to the EVL margin (Fig. 2d) was cut along a 20-μm-long line perpendicular to the margin to reveal circumferential tension (Fig. 2e). Recoil velocities were significantly reduced in YAP;TAZ KD ($n = 50$) compared to control KD embryos ($n = 41$; $11.2 \pm 0.8\ \mu m\ min^{-1}$ vs $23.8 \pm 2.3\ \mu m\ min^{-1}$) (Fig. 2f–h), suggesting reduced actomyosin network tension. Consistent with this, epiboly movements in YAP;TAZ double KD zebrafish embryos were significantly reduced (KD embryos: $53.63 \pm 3.93\%$; control embryos: $70.0 \pm 2.18\%$ deep cell epiboly). To test whether reduced actomyosin network tension is also responsible for neural tube tissue flattening in *hir*, we performed micropipette aspiration experiments[18]. *hir* neural explants were significantly less resistant than WT to external forces applied by aspiration, indicating reduced neural tube tissue tension. The higher deformability of *hir* neural tube tissue was paralleled when myosin activity was reduced by ROCK inhibition (Fig. 2i–k). Together, these analyses indicate that YAP is required for actomyosin-mediated tissue tension in medaka and zebrafish.

Single-cell tracking analysis of the growing neural tube in *hir* showed that tissue flattening was associated with failure to stack cells, and increase in cells slipping to one side after perpendicular cell division (Fig. 3a, Extended Data Figs 4, 5). Live imaging showed loss of filopodia that tether lens to retina during lens invagination[1] (Extended Data Figs 1b, 6a, b). The formation of lens–retina filopodia requires fibronectin (FN)-integrin signalling and contractile actomyosin[1]. While st. 22 WT embryos had elongated thin FN fibrils between invaginating lens and retina, *hir* retina showed punctate FN patches (Fig. 3b1′′, b2′′), suggesting defective FN fibril formation. In addition, large ectopic FN deposits were found on the retina in *hir* (Fig. 3b2′). Similar loss of normal FN fibrils and formation of large FN deposits were observed throughout *hir* embryos (Fig. 3b4′, b5′). Furthermore, integrin β1 accumulation between lens and retina was lost in *hir* (Extended Data Fig. 6c). In contrast, cell–cell adhesion and apical markers, including pan-cadherin, atypical PKC (aPKC) and ZO-1, were unaltered in *hir* (data not shown). Mosaic expression of YAP in *hir* and transplantation experiments both showed that the *hir* mutation acts in a non-cell-autonomous manner (Extended Data Fig. 7, Supplementary Table 4). For instance, in invaginated *hir* lens rescued by mosaic expression of YAP, non-YAP expressing *hir* cells recovered filopodia (Extended Data Figs 7b, 6b). These data suggest that YAP functions in tissue alignment by regulating FN assembly.

To identify downstream YAP effectors regulating tissue tension, we used a human 3D spheroid *in vitro* culture system employing the human retina pigmented epithelial cell line hTERT-RPE1 (RPE1), which displayed a relatively mild proliferation defect upon YAP KD. YAP KD spheroids collapsed upon exposure to external forces by slow centrifugation, unlike normal spheroids (Fig. 4a, b). pMRLC levels were reduced in YAP KD spheroids (Fig. 4c), as in *hir*, suggesting that YAP maintains tissue tension also in human 3D tissues. YAP KD spheroids also lacked the typical beehive-like pattern of FN fibrils and, instead, contained large FN deposits, reminiscent of the *hir* retina phenotype

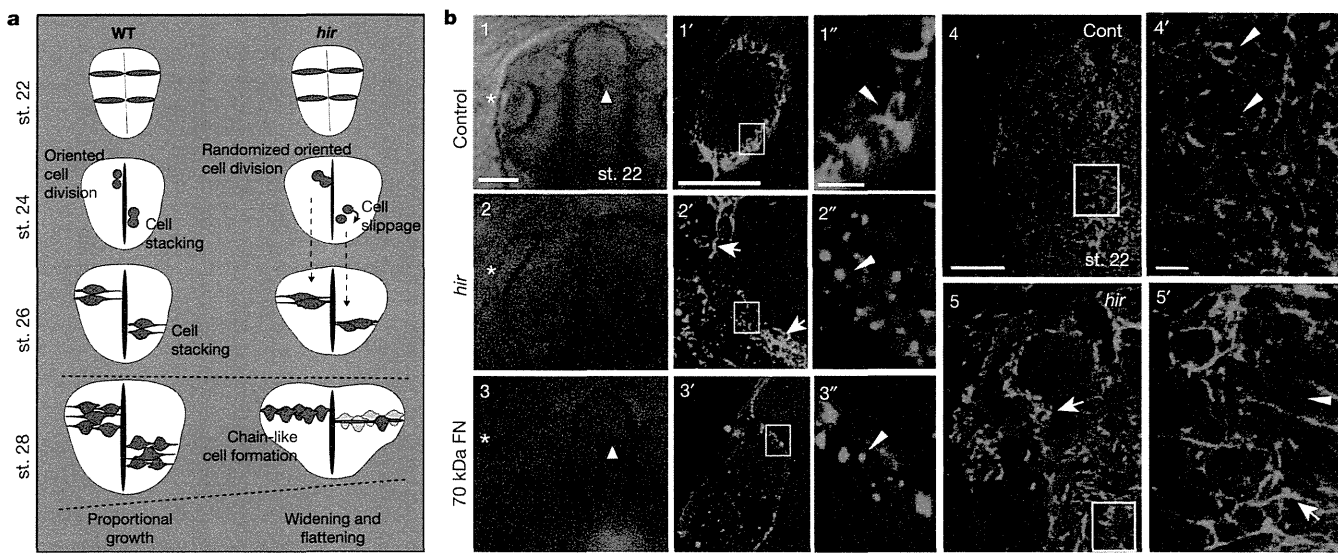

Figure 3 | Cell and tissue dynamics in *hir* mutants. **a**, Schematic: *hir* neural tube collapse is associated with long chain-like arrangements of neuroepithelial cells generated by increased cell slippage and randomized oriented cell division (Extended Data Figs 4, 5). **b**, Whole-mount FN immunohistochemistry (IHC) of st. 22 embryos, dorsal view, anterior to the top. **b1–b1′′**, WT embryos injected with out-of-frame 70 kDa N-terminal medaka FN1a+1b mRNA (250 pg) ($n = 20$); **b2–b2′′**, uninjected *hir* mutants ($n = 11$); **b3–b3′′**, WT embryos injected with N-terminal 70kDa FN1a+1b mRNA (250 pg) ($n = 39$). **b1–b3**, Left anterior head of live embryos (asterisks, lens; triangle, forebrain ventricle); **b1′–b3′**, left eye of FN IHC (green), boxed area magnified in **b1′′–b3′′**; **b4**, **b5**, surface view of FN stained neural tube, WT ($n = 15$) and *hir* ($n = 14$) corresponding to the region in 1 and 2, respectively, boxed area magnified in **b4′** and **b5′**. Arrowheads, FN fibrils/puncta; arrows, FN large deposits. Scale bars, 40 μm in **b1**, **b1′**, **b4**; 5 μm in **b1′′**, **b4′**.

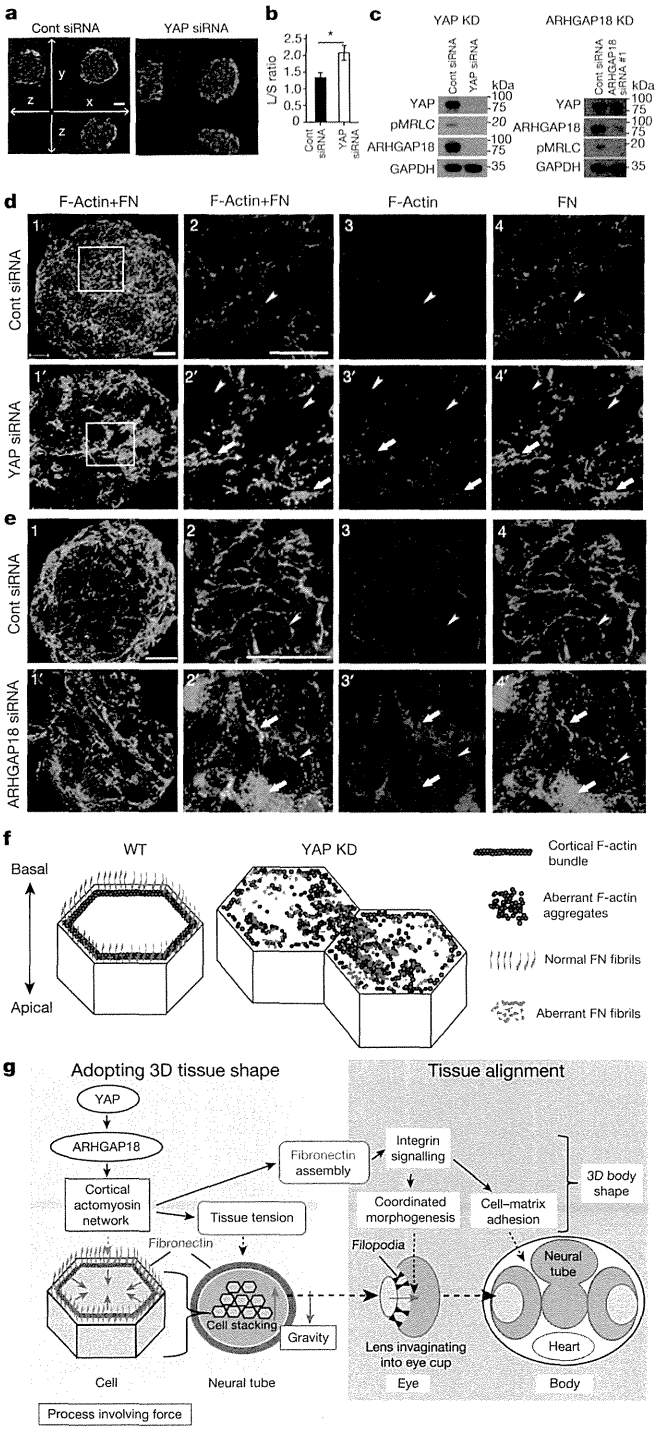

Figure 4 | YAP regulation of tissue tension and FN assembly is mediated by ARHGAP18. **a**, **b**, Confocal 3D sectioning of longest and shortest axes of YAP and control (Cont) KD RPE1 spheroids ($n = 5, 7$) after centrifugation. **b**, Ratio of longest (L)/shortest (S) axes. Error bars, ± s.e.m. $*P < 0.05$, *t*-test (Fig. 4 Source Data). **c**, Immunoblotting of YAP and ARHGAP18 KD spheroids for the indicated proteins (Supplementary Fig. 1). **d**, **e**, Whole-mount imaging of basal surfaces of spheroids transfected with control siRNA ($n = 17$), YAP siRNA ($n = 13$), and ARHGAP18 siRNA ($n = 15$), stained for F-actin (red) and FN (green). **d2**–**d4**, Magnified view of boxed areas in **d1**. Arrowheads, cortical regions; arrows, ectopic F-actin aggregates and aberrant FN fibrils. **f**, Schematic; fine extracellular FN fibrils form in close proximity to cortical F-actin in normal cells, while in YAP and ARHGAP18 KD cells, FN fibrils are reduced and aberrant FN deposits coincide with ectopic F-actin aggregates. **g**, Schematic summarizing how YAP/ARHGAP18-dependent actomyosin network contraction controls tissue shape and alignment. Scale bars, 40 μm in **a**; 30 μm in **d1**, **e1**; 15 μm in **d2**, **e2**.

(Fig. 4d). Cortical actomyosin contraction is required for polymerizing FN monomers to form fibrils[19,20]; consistently, FN fibril formation on the basal surface of control spheroids coincided with cortical F-actin bundles (Fig. 4d). In contrast, loss of normal FN fibrils in YAP KD spheroids was associated with marked reduction of cortical F-actin bundles (Fig. 4d, f). Instead, we observed F-actin aggregates, some of which were associated with large FN deposits, suggesting that they have increased local tension (Fig. 4d). A similar distribution of F-actin and FN was observed in *hir* (Extended Data Fig. 8a). Gene expression profiling of YAP KD spheroids identified only forty genes with reduced expression (see Methods), including *ARHGAP18*, encoding a Rho GTPase activating protein that suppresses F-actin polymerization by inhibiting Rho[21]. *ARHGAP18* transcripts and protein levels were reduced in YAP KD spheroids (Fig. 4c), and ARHGAP18 KD spheroids exhibited a similar phenotype to YAP KD spheroids, including reduced pMRLC levels (Fig. 4c) and aberrant F-actin and FN assembly (Fig. 4e). This suggests that both disruption of cortical F-actin bundles and formation of ectopic F-actin aggregates (Fig. 4f) arise from F-actin over-polymerization in YAP KD spheroids (Extended Data Fig. 8b) and ARHGAP18 KD cells. Together, these results suggest that ARHGAP18 acts downstream of YAP and is required for cortical actomyosin network formation and tissue tension.

To analyse the contribution of actomyosin tension-mediated FN assembly defects to the *hir* eye phenotype, we blocked FN assembly to a similar extent to that in *hir* by overexpressing 70-kDa amino-terminal FN1a and FN1b fragments in WT embryos[22] (Fig. 3b3′, b3′′); this caused near dislocation of the lens and fewer filopodia between lens and retina (Fig. 3b3). *hir* mutants had fewer filopodia than FN assembly blocked embryos (Extended Data Fig. 6a, b), suggesting that contractile actomyosin defects in *hir* exacerbate the incomplete lens dislocation caused by FN assembly defects. In contrast, FN assembly blocked embryos did not exhibit flattened tissues (Fig. 3b1–b3). Furthermore, the medaka FN1 mutant *fukuwarai* (*fku*) also exhibited lens dislocation but not tissue flattening (Extended Data Fig. 8c), suggesting that FN is specifically required for tissue alignment, but not generally for YAP-dependent tissue shape. *ARHGAP18* mRNA levels were significantly reduced in *hir*, and mRNA injection of plasma membrane-targeted myristoylated ARHGAP18 (*myrARHGAP18*) into *hir* substantially rescued FN assembly defects, lens invagination and body flattening (Extended Data Fig. 9a, b). In contrast, inactivation of ARHGAP18 alone was insufficient to produce a recognizable phenotype (data not shown), suggesting that multiple ARHGAP18-related genes function downstream of YAP in medaka embryos. Consistently, short interfering RNA (siRNA) knockdown screening in human cells identified five ARHGAP genes with similar functions to ARHGAP18, homologues of which are conserved in medaka and zebrafish (Extended Data Fig. 9c, d and Supplementary Discussion). These results suggest that ARHGAP18-related genes function as effectors of YAP essential for both tissue shape and FN-dependent tissue alignment. The *hir* phenotype is not simply due to reduced myosin contraction, because injecting mRNA of an activated form of MRLC-DD[23] did not rescue the *hir* phenotype (Extended Data Figs 3a6, b, 8d). Similarly, injection of dominant negative MRLC-AA[23] in WT embryos failed to fully phenocopy the *hir* tissue or body flattening phenotype (Extended Data Fig. 3a5, b). Collectively, these results suggest that YAP function in 3D tissue shape and FN assembly is conserved in human cells and is at least partly mediated by ARHGAP18-related genes.

We propose that YAP is essential for tissue tension, acting through ARHGAP18 and related genes to regulate cortical actomyosin network formation (Fig. 4g). YAP-dependent actomyosin network tension is required for both proper tissue shape and alignment to ensure organ/body shape. Several upstream regulators of YAP-mediated cell proliferation

have been identified, including cellular environment stiffness, suggesting that YAP can function as a mechanosensor[24]. Our data show that YAP also functions as a mechanoregulator of tissue tension. Reduced cortical actomyosin tension is the most probable cause of attenuated tissue tension in *hir* mutants. F-actin over-polymerization perturbs F-actin turnover required for actomyosin contraction in the cytokinetic ring[25]. Our finding that ARHGAP18, a suppressor of F-actin polymerization, functions downstream of YAP further supports a critical role of F-actin polymerization in contractile actomyosin network formation. YAP is required for basal-level actomyosin activity, consistent with ubiquitous expression of actin modulator ARHGAP18[21], additional to which spatiotemporal modulation of actomyosin activity defines tissue shape. Since ARHGAP18 suppresses actin polymerization, which in turn reduces nuclear localization of YAP[26], ARHGAP18 might suppress YAP activity via a negative feedback mechanism. This points to a possible mechanical feedback loop where tissue tension controls YAP, and YAP in turn is required for tissue tension.

Actomyosin contraction promotes FN assembly[27]. The tissue misalignment phenotype in *hir* is most likely owing to failure of YAP-dependent actomyosin contractility in controlling FN assembly. Since FN initiates extracellular matrix organization[27], actomyosin contraction-mediated FN assembly could be a critical *in vivo* mechanism that integrates mechanical signals (for example, tension generated by actomyosin) with biochemical signals (for example, integrin signalling). Notably, the phenotype of YAP KO mouse embryos resembles that of FN KO mouse embryos[28], suggesting that YAP and FN have similar functions in mouse development. Interestingly, while YAP in medaka is predominantly required for tissue tension, its paralogue TAZ seems to be required for cell proliferation (Supplementary Discussion). Given the high degree of conservation of YAP and other Hippo pathway components across metazoa[29], it will be worth investigating whether the extent of tissue three-dimensionality and alignment correlate with the emergence of YAP-mediated resistance to gravity at the evolutionary transition from uni- to multicellular organisms. Finally, generation of a simple organ, such as an eye cup, from induced pluripotent/embryonic stem cells depends on tissue self-organization involving force-mediated processes for which the mechanism remains elusive[30]. Our finding that YAP-dependent force-mediated morphogenesis is required not only for 3D tissue morphogenesis but also tissue alignment suggests that YAP-dependent force-mediated morphogenesis could be involved in self-organization of multiple tissues. Hence, our findings could have implications for the generation of complex organs comprising multiple tissues from induced pluripotent/embryonic stem cells.

Online Content Methods, along with any additional Extended Data display items and Source Data, are available in the online version of the paper; references unique to these sections appear only in the online paper.

Received 26 August; accepted 29 December 2014.
Published online 16 March 2015.

1. Chauhan, B. K. *et al.* Cdc42- and IRSp53-dependent contractile filopodia tether presumptive lens and retina to coordinate epithelial invagination. *Development* **136,** 3657–3667 (2009).
2. Nelson, C. M. & Bissell, M. J. Of extracellular matrix, scaffolds, and signaling: tissue architecture regulates development, homeostasis, and cancer. *Annu. Rev. Cell Dev. Biol.* **22,** 287–309 (2006).
3. Mammoto, T. & Ingber, D. E. Mechanical control of tissue and organ development. *Development* **137,** 1407–1420 (2010).
4. Thompson, D. W. *On Growth and Form* (Cambridge Univ. Press, 1917).
5. Furutani-Seiki, M. *et al.* Neural degeneration mutants in the zebrafish, *Danio rerio*. *Development* **123,** 229–239 (1996).
6. Furutani-Seiki, M. *et al.* A systematic genome-wide screen for mutations affecting organogenesis in medaka, *Oryzias latipes*. *Mech. Dev.* **121,** 647–658 (2004).
7. Sudol, M. *et al.* Characterization of the mammalian YAP (Yes-associated protein) gene and its role in defining a novel protein module, the WW domain. *J. Biol. Chem.* **270,** 14733–14741 (1995).
8. Pan, D. The Hippo signaling pathway in development and cancer. *Dev. Cell* **19,** 491–505 (2010).
9. Zhao, B., Tumaneng, K. & Guan, K.-L. L. The Hippo pathway in organ size control, tissue regeneration and stem cell self-renewal. *Nature Cell Biol.* **13,** 877–883 (2011).
10. Miesfeld, J. B. & Link, B. A. Establishment of transgenic lines to monitor and manipulate Yap/Taz-Tead activity in zebrafish reveals both evolutionarily conserved and divergent functions of the Hippo pathway. *Mech. Dev.* **133,** 177–188 (2014).
11. Gee, S. T., Milgram, S. L., Kramer, K. L., Conlon, F. L. & Moody, S. A. Yes-associated protein 65 (YAP) expands neural progenitors and regulates Pax3 expression in the neural plate border zone. *PLoS ONE* **6,** e20309 (2011).
12. Lei, Q. Y. *et al.* TAZ promotes cell proliferation and epithelial-mesenchymal transition and is inhibited by the Hippo pathway. *Mol. Cell. Biol.* **28,** 2426–2436 (2008).
13. Zhao, B., Li, L., Tumaneng, K., Wang, C. Y. & Guan, K.-L. L. A coordinated phosphorylation by Lats and CK1 regulates YAP stability through $SCF^{\beta\text{-}TRCP}$. *Genes Dev.* **24,** 72–85 (2010).
14. Heisenberg, C.-P. P. & Bellaïche, Y. Forces in tissue morphogenesis and patterning. *Cell* **153,** 948–962 (2013).
15. Vicente-Manzanares, M., Ma, X., Adelstein, R. S. & Horwitz, A. R. Cytoskeletal motors: non-muscle myosin II takes centre stage in cell adhesion and migration. *Nature Rev. Mol. Cell Biol.* **10,** 778–790 (2009).
16. Köppen, M., Fernández, B. G., Carvalho, L., Jacinto, A. & Heisenberg, C.-P. P. Coordinated cell-shape changes control epithelial movement in zebrafish and *Drosophila*. *Development* **133,** 2671–2681 (2006).
17. Behrndt, M. *et al.* Forces driving epithelial spreading in zebrafish gastrulation. *Science* **338,** 257–260 (2012).
18. Guevorkian, K., Colbert, M.-J., Durth, M., Dufour, S. & Brochard-Wyart, F. Aspiration of biological viscoelastic drops. *Phys. Rev. Lett.* **104,** 218101 (2010).
19. Singh, P., Carraher, C. & Schwarzbauer, J. E. Assembly of fibronectin extracellular matrix. *Annu. Rev. Cell Dev. Biol.* **26,** 397–419 (2010).
20. Rolo, A., Skoglund, P. & Keller, R. E. Morphogenetic movements driving neural tube closure in *Xenopus* require myosin IIB. *Dev. Biol.* **327,** 327–338 (2009).
21. Maeda, M. *et al.* ARHGAP18, a GTPase-activating protein for RhoA, controls cell shape, spreading, and motility. *Mol. Biol. Cell* **22,** 3840–3852 (2011).
22. McDonald, J. A. *et al.* Fibronectin's cell-adhesive domain and an amino-terminal matrix assembly domain participate in its assembly into fibroblast pericellular matrix. *J. Biol. Chem.* **262,** 2957–2967 (1987).
23. Iwasaki, T., Murata-Hori, M., Ishitobi, S. & Hosoya, H. Diphosphorylated MRLC is required for organization of stress fibers in interphase cells and the contractile ring in dividing cells. *Cell Struct. Funct.* **26,** 677–683 (2001).
24. Dupont, S. *et al.* Role of YAP/TAZ in mechanotransduction. *Nature* **474,** 179–183 (2011).
25. Pinto, I. M., Rubinstein, B., Kucharavy, A., Unruh, J. R. & Li, R. Actin depolymerization drives actomyosin ring contraction during budding yeast cytokinesis. *Dev. Cell* **22,** 1247–1260 (2012).
26. Sansores-Garcia, L. *et al.* Modulating F-actin organization induces organ growth by affecting the Hippo pathway. *EMBO J.* **30,** 2325–2335 (2011).
27. Daley, W. P., Peters, S. B. & Larsen, M. Extracellular matrix dynamics in development and regenerative medicine. *J. Cell Sci.* **121,** 255–264 (2008).
28. Morin-Kensicki, E. M. *et al.* Defects in yolk sac vasculogenesis, chorioallantoic fusion, and embryonic axis elongation in mice with targeted disruption of Yap65. *Mol. Cell. Biol.* **26,** 77–87 (2006).
29. Hilman, D. & Gat, U. The evolutionary history of YAP and the Hippo/YAP pathway. *Mol. Biol. Evol.* **28,** 2403–2417 (2011).
30. Sasai, Y. Cytosystems dynamics in self-organization of tissue architecture. *Nature* **493,** 318–326 (2013).

Supplementary Information is available in the online version of the paper.

Acknowledgements We thank M. Raff, T. Perry, A. Ward, M. Wills, J. Caunt, J. Clarke, L. Hurst and C. Tickle for critical reading and comments. We thank M. Tada, M. Furuse, N. Wada, Y. Nakai, J. Robinson and R. Kelsh for contributions to the paper and University of Bath for fish and bioimaging facilities. This work was funded by the ERATO/SORST projects of JST, Japan (H.K.), National Institutes of Health R01EY014167 (B.A.L.) and Medical Research Council, UK (M.F.-S.).

Author Contributions S.P., H.W., Y.A., M.B., T.M., H.M., S.H., T.S., S.F.G.K., Y.O., S.A., A.M., S.L., J.B.M., B.A.L., T.S., A.C.M., A.O.U., S.B. and M.F.-S. performed experiments. S.P., H.W., Y.A., M.B., T.M. and M.F.-S. conceived the study. S.B., N.S., H.N., S.M., H.K., C.-P.H., H.N. and M.F.- S. supervised the study. C.-P.H. and M.F.- S. wrote the paper. All authors interpreted data.

Author Information Reprints and permissions information is available at www.nature.com/reprints. The authors declare no competing financial interests. Readers are welcome to comment on the online version of the paper. Correspondence and requests for materials should be addressed to C.-P.H. (heisenberg@ist.ac.at), H.N. (nishina.dbio@mri.tmd.ac.jp) or M.F.-S. (furutaniseiki@gmail.com).

METHODS

Fish maintenance and fish strains. Medaka (*Oryzias latipes*) and zebrafish (*Danio rerio*) strains were maintained and raised according to previously published procedures[31]. Medaka and zebrafish embryos were raised in E3 solution at 28 °C. Fish care and procedures were approved by the University of Bath Ethical Review Committee, and are in compliance with the Animals Scientific Procedures Act 1986 of the UK. Medaka WT strains K-Cab, K-Kaga, and the mutant strain *hir*$^{54\text{-}20C}$,*fku*$^{8\text{-}33A}$, were used[6]. Zebrafish WT strain AB and *Tg(actb2:myl12.1-eGFP)*[32], that allow visualization of myosin, were used.

Embryological experiments. For fixation and live imaging, embryos were anaesthetized with 0.01% tricaine. For live imaging, embryos were embedded in 0.8% low melting temperature agarose (Type IV-A, Sigma, USA) in 35 mm glass-base dishes (Iwaki, Japan) at 28 °C. Standard embryological procedures including, dechorionation, fixation, *in situ* hybridization, immunohistochemistry, microinjection and cell transplantation were carried out according to previously published procedures[31]. Cells were transplanted to the region fated to become the eye and Cuvier's duct according to our fate map[33].

Positional cloning of *hir*. The *hir* mutation induced in the K-Cab strain was crossed with the polymorphic K-Kaga strain to carry out genetic mapping according to a previously published procedure[34]. To map the *hir* mutation on the chromosome, bulked segregant analysis was performed using M-markers[35] on DNA isolated from 48 homozygous mutant embryos and 48 WT siblings from F_2 embryos of mutant × K-Kaga mapping crosses.

Chromosome walking on chromosome 13 was performed using restriction fragment length polymorphism markers between K-Cab and K-Kaga strains to map to the two BAC clones. For fine mapping, 1,908 meioses were analysed to identify 9 recombinants mapping *hir* mutation close to *YAP*. *YAP* complementary DNA was amplified from *hir* mutants by RT–PCR and sequenced directly to identify the mutation.

RT–PCR cDNA cloning and construction. Total RNAs were isolated using TRIzol (Life Technologies) and were converted to cDNA using the RNA-PCR kit ver.3 (Takara Bio, Japan) followed by PCR using KOD plus polymerase (Toyobo, Japan). For mRNA production, PCR amplified full-length cDNAs (medaka *YAP, 70KDaFN1a,b, ARHGAP18*) were cloned into pCS2+ and for *in situ* hybridization medaka *sox3* cDNA was cloned into pBluescript II SK(−). *pCS2+myr-ARHGAP18* was constructed by adding the myristoylation sequence using oligonucleotides to produce myristoylated *ARHGAP18* mRNA. mRNAs were synthesized using SP6 mMESSAGE mMACHINE Kit (Ambion, USA). Primer sequences are shown in Supplementary Table 5.

Gravity experiment. Dechorionated embryos were embedded in 0.8% low melting temperature agarose in three orientations against gravity at st. 17, fixed at st. 25 and subjected to cryosectioning to determine the direction of tissue/organ collapse. Collapse of embryos towards gravity was assessed using images of sections stained with TO-PRO-3 and phalloidin.

Microinjection. mRNA, DNA and Morpholino were injected at 1-cell or 8-cell stages to deliver them to all cells or in a mosaic manner. The volume of one-shot of injection was 0.5 nl.

Phenotypic rescue experiments. Embryos from *hir*$^{+/-}$ heterozygote crosses were injected with mRNA of YAP variants. For transplantation phenotypic rescue experiments, embryos were genotyped by PCR using primers (Supplementary Table 5).

Morpholino KD analysis in medaka and zebrafish. Morpholino oligonucleotide (MO) from Gene Tools (USA) were used (Supplementary Table 6). Specificity of KD by MO was confirmed in a slightly different manner in medaka and zebrafish. Since rescue of the phenotype by mRNA injection did not work effectively in zebrafish, three different types of MOs, translation blocking (TB), splicing blocking (SB) and 5′ UTR MOs, were used and all were confirmed to induce a similar phenotype. In medaka, TB and SB MOs were used, and the phenotype was rescued by co-injecting corresponding mRNAs. To determine efficiency of KD, semiquantitative RT–PCR was carried out using primers that distinguish defective splicing from normal forms of mRNA (Supplementary Table 5).

Immunohistochemistry. Embryos were fixed in either 4% paraformaldehyde (PFA), Dent fixative or 1% TCA for 1–3 days and subjected to cryosectioning as described previously[31]. Antibodies used were: anti-FN antibody (Ab), Sigma F3648 at 1:100; β-integrin monoclonal Ab, 8c8 (Developmental Studies Hybridoma Bank, USA) at 1:10; anti-aPKC C-20 (SC216, Santa Cruz Biotech, USA) at 1:100; anti-PCNA (PC10, Santa Cruz Biotech, USA) at 1:500; anti-laminin (Ab-1, NeoMarkers, USA) at 1:100 and anti-ZO-1[36] (gift from M. Itoh) at 1:1. Sections were counterstained with Alexa Fluor 488 or 546 Phalloidin (A12379, A22283, Invitrogen USA) at 1:250 and TO-PRO-3 (T3605, Invitrogen, USA) at 1:1,000.

Time-lapse microscopy and image analysis. Time-lapse analysis of lens dislocation was carried out using a Leica MZ16FA dissecting microscope. Confocal microscopy used a Leica TCS SP5 and images were analysed by Imaris 7.3 (Bitplane, ANDOR Technology, UK) and Amira 5.1 (Visage Imaging, USA). Cell division orientation (θ) of telophase cells in time-lapse sequences was determined by drawing an axis from the ventricular zone-attached non-moving daughter cell (asterisk Extended Data Fig. 5c) towards the non-attached moving daughter cell[37]. The acute angle of this axis was then measured against the axis of the ventricular zone. Imaging was carried out dorsal side down using an inverted microscope. Rose diagrams were generated using Oriana v4 (Kovach Computing Services, UK).

Spheroid analysis. hTERT-RPE1 cells (American Type Culture Collection; CRL-4000) were seeded (2×10^5 cells per well in 6-well plates). Each stealth RNA (100 pmol) of Opti-Mem medium (Life Technologies) was transfected using Lipofectamine RNAi Max (Life Technologies) followed by incubation for 24 h at 37 °C. Trypsin treatment was used to collect RNAi-transfected cells from wells which were resuspended in 2 ml of 10% FBS (Hyclone, ThermoFisher Scientific)-DMEM. These resuspensions were seeded to 6 wells of a 12-well plate (Hydrocell, CellSeed Japan) and incubated for 48 h at 37 °C. Spheroids were fixed in 3% formalin and subjected to immunostaining. Reagents used for immunostaining: anti-β-catenin (BD transduction, 610154, 1:200), anti-FN (Sigma F3648, 1:500), Alexa Fluor 546 Phalloidin (Invitrogen, A22283,1:200). For the list of primers see Supplementary Table 5.

Western blotting. Spheroids were lysed in lysis buffer (0.5% TritonX-100, 150 mM NaCl, 20 mM Tris-HCl pH 7.5). The lysates were sheared with a 21-gauge needle, incubated on ice for 30 min and clarified by centrifugation at 20,817*g* for 15 min at 4 °C. The extracted proteins were separated by SDS–PAGE and transferred to immobilon transfer membrane (Millipore) for western blotting analyses. The primary antibodies were anti-YAP1 pAb (4912 Cell Signaling, 1:500), anti-fibronectin pAb (F3648, Sigma Aldrich, 1:1,000), anti-ARHGAP18 pAb (1:10,000)[17,21], anti-MYH9 pAb (3403 Cell Signaling, 1:1,000), anti-Phospho Ser1943-MYH9 pAb (5026 Cell Signaling, 1:1,000), anti-MYH10 mAb (8824 Cell Signaling, 1:1,000), anti-Phospho-Ser19 MLC2 (3675, Cell Signaling, 1:100), and anti-GAPDH mAb (sc32233, Santa Cruz, 1:5,000).

Actomyosin tension measurement by laser cutting. Laser cutting experiments were carried out using a UV-laser ablation system as previously described[17]. Tg(*actb2:myl12.1-eGFP*)[32] embryos were mounted in 1% low melting point agarose (Invitrogen) embedded in E3 medium inside a glass bottom Petri dish (Mattek). A 63× water immersion objective (NA = 1.2, Zeiss) was used to visualize the YSL actomyosin ring at respective epiboly stages. Cuts were made at a distance of 20 μm from the EVL/YSL boundary by applying 25 UV pulses at 1 kHz to 40 equidistant sites along a 20-μm-long line perpendicular to the EVL margin as depicted in Fig. 2e. Fluorescent images of embryos were captured using an iXon DU-897-BV camera (Andor Technology) with a 380 ms exposure time and 500 ms frame rate (LabVIEW v10.0.1). The ablation procedure itself took 1.2 s during which no images were acquired. Temperature was kept constant at 28.5 ± 1 °C throughout the experiment by means of a custom-built temperature chamber and an objective heating ring. The recoil velocity of the cortex in response to the cut opening was analysed using customized Matlab (v7.12) scripts based on particle image velocimetry (PIV) as previously described[17,38]. The component of the PIV flow field that is orthogonal to the cut line was averaged in two adjacent rectangles (Fig. 2f) for time frames up to 9 s post-ablation. The resulting recoil velocity curves for single embryo ablation experiments were averaged to yield the mean temporal recoil velocity curve for the depicted conditions (Fig. 2g). Laser ablation experiments that caused wound response recognizable by a strong accumulation of myosin following the ablation were discarded from the analysis. In these experiments leakage of yolk cytoplasm through a membrane opening may interfere with the cortical tension measurements[17].

Micropipette aspiration analysis. The whole neural tube was dissected out from st. 22 medaka embryos and was cut using a tungsten needle at the level of diencephalon-midbrain boundary. The micropipette was connected to a Microfluidic Flow Control System (Fluigent, Fluiwell) which was controlled via a custom-programmed Labview (National Instruments) interface. In the BSS medium, the neural tube was aspirated from the open end by a micropipette (internal radius = 30–35 μm) at a constant pressure (ΔP = 4.5 mbar) for 10 min. Aspiration was imaged at 500 ms intervals by a Leica SP5 inverted confocal microscope using a Leica 20×, 0.7 NA objective. Temperature in the dish was kept constant at 28 °C by a heated sample holder. Measuring the tongue length of the tissue within the micropipette using FIJI software over time yielded the characteristic tissue flow curves during aspiration for WT and *hir* mutant neural tube explants. To reduce cortical tension WT neural tube explants were treated with ROCK inhibitor Y27632 (250 μM dissolved in water) for 15 min before performing the micropipette aspiration experiment.

Oligo DNA microarray analysis. For the Oligo DNA microarray analysis, total RNA samples were collected from hTERT-RPE1 multicellular spheroids. 3D-Gene Human Oligo chip 25k (TORAY) was used. Total RNA of YAP siRNA-transfected spheroids and that of negative control siRNA were labelled with Cy3 or Cy5 using the Amino Allyl MessageAMP II aRNA Amplification Kit (Life Technologies), respectively. The Cy3- or Cy5-labelled aRNA pools and hybridization buffer were mixed, and hybridized for 16 h at 37 °C. The hybridization was performed using

the supplier's protocols (http://www.3d-gene.com). Hybridization signals were scanned using a 3D-Gene Scanner 3000 (TORAY). Detected signals for each gene were normalized by a global normalization method (Cy3/Cy5 ratio median = 1). Genes with Cy3/Cy5 normalized ratios greater than 2.0 or less than 0.5 were defined, respectively, as commonly up- or downregulated genes. The results were deposited at GEO under the accession number GSE54146.

Quantitative RT–PCR analysis. Total RNA was isolated from WT and *hir* mutant embryos at various developmental stages using TRIzol (Invitrogen) according to the manufacturer's instructions. First-strand cDNA was synthesized from 1 μg total RNA using Superscript III reverse transcriptase (Invitrogen) with an oligo-dT primer. Each quantitative real-time RT–PCR was performed using the CFX96 real-time PCR detection system (Bio-Rad). Primers used for RT–PCR analysis are shown in Supplementary Table 5. For a 10 μl PCR, cDNA template was mixed with the primers to final concentrations of 250 nM and 5 μl of SsoFast EvaGreen Supermix (Bio-Rad), respectively. The reaction was first incubated at 95 °C for 3.5 min, followed by 45 cycles at 95 °C for 30 s, 65 °C for 30 s and 72 °C for 30 s.

Phylogenetic analysis of ARHGAP18-related genes in 11 metazoan species. Lists of homologues of ARHGAP18 family (TF314044) and its closely related families ARHGAP6 (TF316710) and ARHGAP11 (TF332212) in 11 metazoan model species were downloaded from the Treefam database. Amino-acid sequences for these genes were downloaded from Ensembl. Multiple sequence alignment was performed using the PRANK package. This alignment was used to infer the phylogenetic relationship of these genes using maximum likelihood using FastTree 2.1.

ARHGAP siRNA screening in HeLa cell line. A library of siRNAs targeting human GAPs was obtained from Invitrogen. HeLa cells cultured in 24-well plates were transfected with siRNAs (20 nM) using Lipofectamine RNAiMAX. After 72 h, cells were fixed with 4% PFA and stained with FITC-labelled phalloidin (Invitrogen). Images were taken using an Olympus IX71 fluorescence microscope.

Statistical analyses. Statistical significance between WT and mutant groups was tested using independent two-tailed *t*-tests (for two-way comparisons) and one-way ANOVAs (for multiple comparisons), with a Dunnett's T3 post-hoc where necessary, in SPSS 20 (IBM) or Prism v5.0 (GraphPad). The Dunnett's T3 post-hoc assumes variances to be unequal and allows comparisons of groups with different *n* numbers. To test for differences in mitotic orientation between WT and *hir* we performed the Kolmogorov–Smirnov (KS) test (http://www.physics.csbsju.edu/stats/KS-test.n.plot_form.html). The KS test makes no assumptions about the distribution of data being tested. Sample size was not pre-determined. We repeated experiments a minimum of three times with sufficient *n* numbers for each repeat to be confident that reported results are representative. Randomization was not applied to allocate embryos to experimental groups. Blinding to group allocation was not used. Error bars on graphs show ± standard error of the means (s.e.m.), except when stated otherwise. Data points that deviated by more than ± 3× the standard deviation of the sample mean were excluded from analysis.

***P* values and sample sizes.** *P*-values vs WT unless specified. Fig. 1c: $n_{cont} = 39$, $n_{hir} = 25$ ($P = < 0.001$), $n_{mYAPKDhir} = 24$ ($P = < 0.001$), $n_{mYAPKDhir+YAPmRNA} = 22$ ($P = 1.000$). Fig. 2b: $n_{WT} = 26$, $n_{hir} = 14$ ($P = 0.0001$). Fig. 4b: $n_{contsiRNA} = 7$, $n_{YAPsiRNA} = 5$ ($P = 0.023$). Extended Data Fig. 2h: $n_{contMO} = 20$, $n_{ZFYAPTBMO} = 11$ ($P = < 0.001$), $n_{ZFYAP;TAZTB} = 10$ ($P = < 0.001$). Extended Data Fig. 2i: n_{WT} st. 20 = 5, st. 22 = 8, st. 24 = 13, st. 26 = 6, st. 28 = 10, n_{hir} st. 20 = 8, st. 22 = 4, st. 24 = 6, st. 26 = 9 ($P = 0.0284$), st. 28 = 5 ($P = 0.0088$), n_{TAZMO} st. 20 = 5, st. 22 = 5, st. 24 = 10, st. 26 = 12, st. 28 = 12. Extended Data Fig. 2j: n_{WT} st. 20 = 11, st. 22 = 7, st. 24 = 10, st. 26 = 11, st. 28 = 11, n_{hir} st. 20 = 7, st. 22 = 7, st. 24 = 11, st. 26 = 13 ($P = 0.0158$ vs TAZMO st. 26), st. 28 = 7 ($P = 0.0075$ vs TAZMO st. 28), n_{TAZMO} st. 20 = 5, st. 22 = 5, st. 24 = 10 ($P = 0.0007$), st. 26 = 8 ($P = 0.0008$), st. 28 = 6 ($P = 0.0120$). Extended Data Fig. 3b: $n_{WT} = 174$, $n_{hir} = 70$ ($P = < 0.001$), $n_{mYAPKDhir} = 85$ ($P = < 0.001$), $n_{MRLCAA > WT} = 135$ ($P = < 0.001$), $n_{MRLCDD>hir} = 92$ ($P = 0.1830$ vs *hir*). Extended Data Fig. 4b: $n_{WT} = 3$, $n_{hir} = 3$. Extended Data Fig. 5b: n_{WT} cell stacking = 9, cell slippage = 8, parallel division = 5, n_{hir} cell stacking = 3 ($P = <0.01$), cell slippage = 21 ($P = <0.05$), parallel division = 5. Extended Data Fig. 5d: KS-test, $P = 0.01$, n_{WT} st. 22–24 = 32, st. 25–26 = 13, n_{hir} st. 22–24 = 14, st. 25–26 = 20. Extended Data Fig. 6b: $n_{WT} = 10$, $n_{70kDaFN>WT} = 13$ ($P = 0.0032$), $n_{hir} = 6$ ($P = 0.0001$), $n_{YAPS87A>hir} = 10$ ($P = 0.0013$ vs *hir*).

31. Porazinski, S. R., Wang, H. & Furutani-Seiki, M. Essential techniques for introducing medaka to a zebrafish laboratory–towards the combined use of medaka and zebrafish for further genetic dissection of the function of the vertebrate genome. *Methods Mol. Biol.* **770,** 211–241 (2011).
32. Maître, J.-L. *et al.* Adhesion functions in cell sorting by mechanically coupling the cortices of adhering cells. *Science* **338,** 253–256 (2012).
33. Hirose, Y. Varga, Z. M., Kondoh, H. & Furutani-Seiki, M. Single cell lineage and regionalization of cell populations during Medaka neurulation. *Development* **131,** 2553–2563 (2004).
34. Iwanami, N. *et al.* WDR55 is a nucleolar modulator of ribosomal RNA synthesis, cell cycle progression, and teleost organ development. *PLoS Genet.* **4,** e1000171 (2008).
35. Naruse, K. *et al.* A medaka gene map: the trace of ancestral vertebrate proto-chromosomes revealed by comparative gene mapping. *Genome Res.* **14,** 820–828 (2004).
36. Itoh, M., Nagafuchi, A., Moroi, S. & Tsukita, S. Involvement of ZO-1 in cadherin-based cell adhesion through its direct binding to alpha catenin and actin filaments. *J. Cell Biol.* **138,** 181–192 (1997).
37. Alexandre, P., Reugels, A. M., Barker, D., Blanc, E. & Clarke, J. D. Neurons derive from the more apical daughter in asymmetric divisions in the zebrafish neural tube. *Nature Neurosci.* **13,** 673–679 (2010).
38. Mayer, M., Depken, M., Bois, J. S., Jülicher, F. & Grill, S. W. Anisotropies in cortical tension reveal the physical basis of polarizing cortical flows. *Nature* **467,** 617–621 (2010).

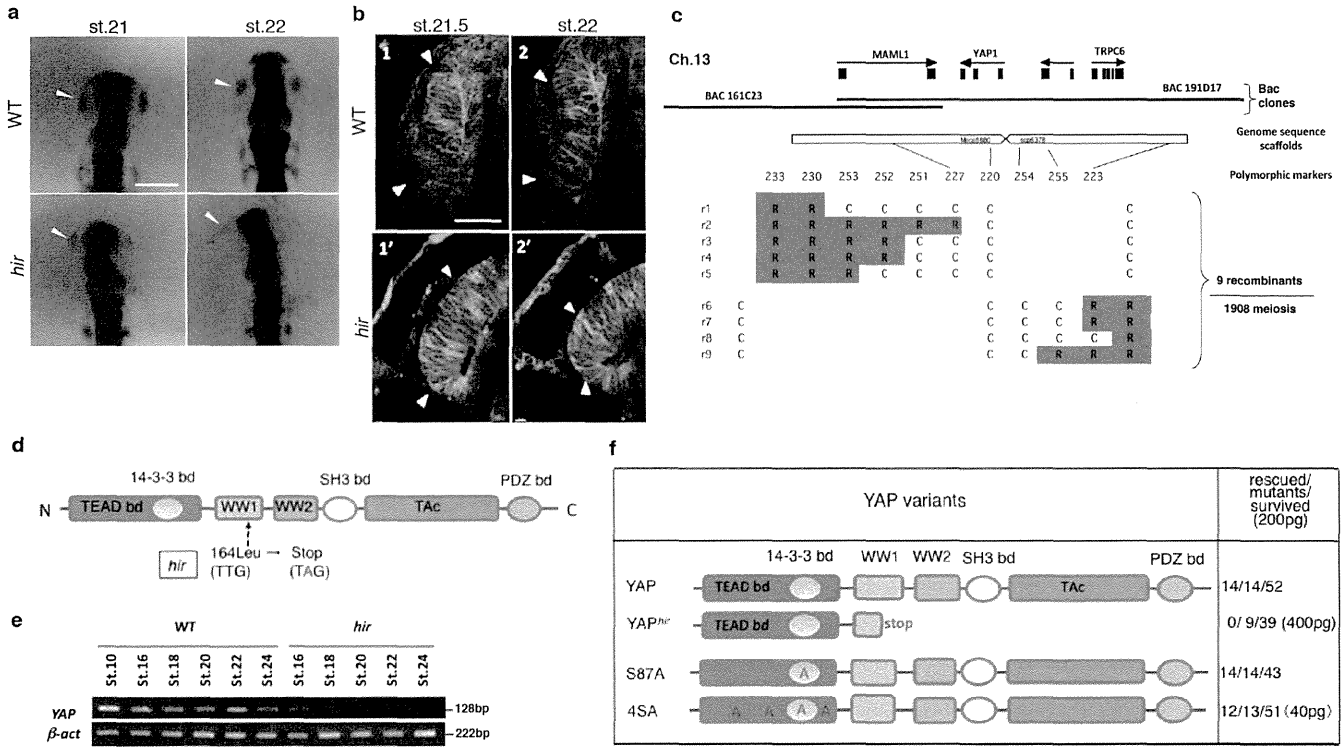

Extended Data Figure 1 | YAP is mutated in *hir* mutants. **a**, *In situ* hybridization of *sox3* showed that the lens placode (arrowhead) is specified in *hir* mutant embryos ($n = 3$) at st. 21. At st. 22, the nascent lens invaginated in WT ($n = 21$), but not in *hir* mutant embryos ($n = 13$, arrowhead). **b**, Two frames from time-lapse imaging of retina of embryos injected with membrane EGFP and nuclear red fluorescent protein (MNFP) mRNAs. In WT ($n = 10$), the nascent lens invaginates from st. 21 (**b1**, margins of the lens indicated by arrowheads with retina to the right), whereas in *hir* ($n = 7$) the lens mostly detached from the retina (**b2′**, arrowheads show lens remnants attached to the retina). Scale bars, 80 μm in **a**; 30 μm in **b**. **c**, Nine recombinants in 1,908 meiosis mapped *hir* close to the YAP gene on chromosome 13 (R: recombinant, C: non-recombinant embryos). **d**, YAP cDNA encodes six protein binding domains/motifs and one transcription activation (TAc) domain; a non-sense mutation in WW1 domain in *hir*. **e**, RT–PCR analysis of YAP mRNA during development. *β-actin* as control. **f**, mRNA of normal YAP and its variants were injected into *hir* mutants. The numbers represent: *hir* phenotype rescue judged via brain thickness, heart migration and Cuvier's duct formation; mutants (judged by genotyping when necessary); survived injected embryos of $hir^{+/-}$ crosses. High dose (400 pg) mRNA of YAP^{hir} variant was injected into WT embryos to examine dominant-negative effects. The rescue by YAP^{4SA} variant required only 20% of the amount required to rescue using normal *YAP* mRNA.

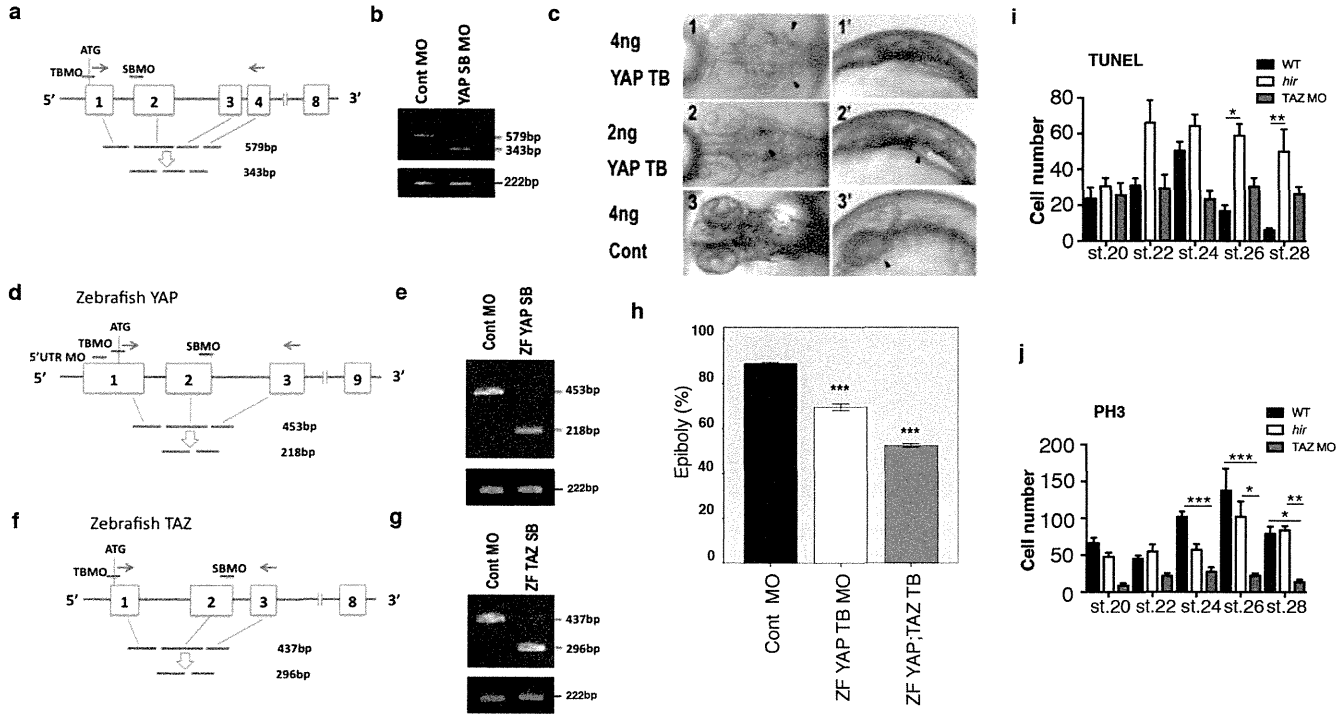

Extended Data Figure 2 | Morpholino knockdown in medaka and zebrafish. **a**, Design of medaka YAP TB and SB MOs relative to translation start (ATG), exons (numbered boxes) and introns. Primers (arrows) used to assess the efficiency of SB MO KD. **b**, Upper panel, proper splicing of YAP transcripts (579 bp) was nearly fully blocked (343 bp, <5% of normal level) by YAP SB MO (5 ng), assessed by RT–PCR; lower panel, *β-actin* control. **c**, WT embryos injected with YAP TB MO and standard control MO. **c1**–**c3** Dorsal and **c1′**–**c3′** lateral views (also Supplementary Table 1). Arrowheads indicate location of heart progenitors. Body flattening and bilateral cardiac progenitor cell migration was affected in a dose-dependent manner. **c2**, **c2′**, Bilateral cardiac progenitor cells fused at the midline but did not migrate anteriorly; **c1**, **c1′** their migration arrests next to the ears at the high dose. The two distinct YAP morpholinos (YAP TB and SB MOs) mimicked the *hir* phenotype (*hir* mutants have a *cardia bifida* phenotype (arrowheads in Fig. 1a1 and a1′)) in a dose-dependent manner. To further verify specificity of the YAP MOs, YAP TB MO was co-injected with human YAP mRNA that does not hybridize with the YAP TB MO. Injection of YAP TB (but not YAP SB) MO into *hir* mutant embryos enhanced the blastopore closure phenotype of *hir* mutants (Fig. 1b, c, Supplementary Table 2). These maternal YAP KD *hir* mutant embryos failed to close the blastopore. Less than half the amount (2 ng) of YAP TB MO was required for causing this phenotype in *hir* mutants compared to that required for WT embryos (5 ng). This blastopore closure phenotype was rescued by medaka YAP mRNA (200 pg) co-injection. **d**–**g**, Zebrafish (ZF) WT embryos injected with three distinct ZFYAP MOs (TB, 5′ UTR and SB) exhibit the blastopore closure phenotype as in medaka (Supplementary Table 3). Efficiencies of ZF YAP and TAZ SB MO KD (1.5 ng each) were assessed by RT–PCR using primers in **d**, **f**, respectively as in **a**, **b**. As reported by Gee *et al.*, co-injection of ZF YAP mRNAs did not rescue the ZF YAP MO phenotype in zebrafish[11]. **h**, Co-injection of ZF TAZ MO (total 2 ng) enhanced slow epiboly of YAP TB KD-injected embryos; control = 89 ± 4.16% ($n = 20$), YAP KD = 70.09 ± 4.7% ($n = 11$), YAP/TAZ KD = 52.5 ± 2.64% ($n = 10$). Error bars show ± s.e.m. $^{***}P < 0.001$, one-way ANOVA. *y* axis shows percentage epiboly. **i**, **j**, TUNEL for cell death and phosphohistone H3 (PH3) antibody staining for cell proliferation (see methods for sample sizes). Stained cells in the neural tube were counted. Error bars indicate ± s.e.m. $^{*}P < 0.05$, $^{**}P < 0.01$, $^{***}P < 0.001$, one-way ANOVA.

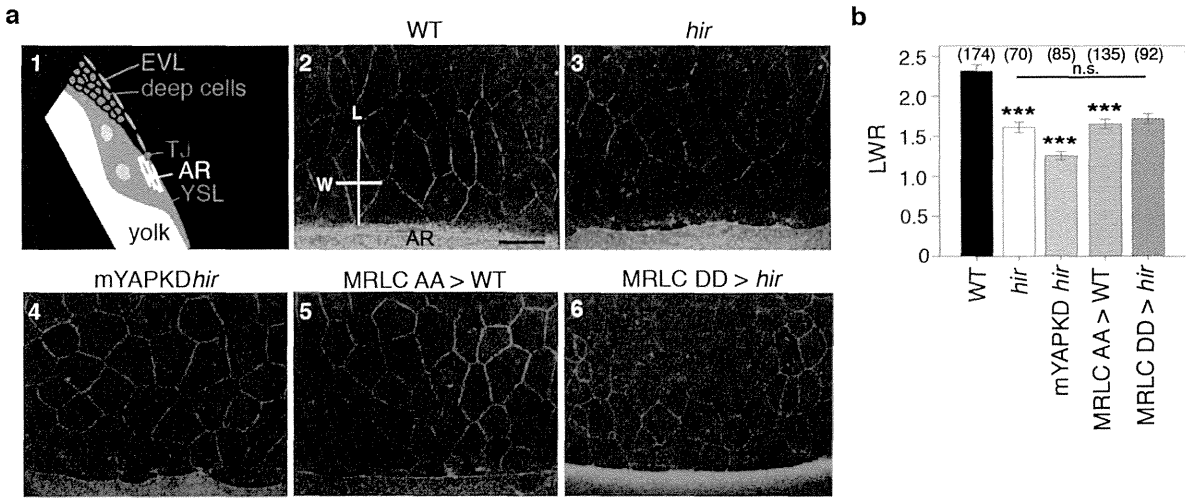

Extended Data Figure 3 | Anisotropic enveloping layer cell shape analysis in *hir* mutants. **a1**, Schematic of sectional view of blastoderm margin of a gastrulating embryo (TJ, tight junction; AR actomyosin ring; YSL, yolk syncytial layer; EVL, enveloping layer); **a2–a6**, EVL shape was visualized in phalloidin-stained fixed medaka embryos at 75% epiboly (st. 16, 21 hpf) and compared among, 2 WT ($n = 14$); 3 *hir* ($n = 9$); 4 maternal YAP KD *hir* mutants (mYAPKD*hir*) by TB MO-injection into *hir* embryos ($n = 12$), 5 MRLC-AA (dominant negative form) mRNA-injected WT ($n = 6$); and 6, MRLC-DD (constitutive active form) mRNA-injected *hir* embryos ($n = 4$). **b**, EVL shape anisotropy quantification by the length/width ratio (LWR, shown in **a2**) of marginal EVL cells (up to 4 rows back from the EVL/YSL boundary, shown in Fig. 2d bracket). While EVL shape anisotropy was reduced in *hir* mutant embryos (**a3**) to a level comparable to that of MRLC blocked embryos (**a5**), activation of MRLC in *hir* (**a6**) did not rescue it. Parentheses indicate number of cells measured. Scale bar 30 μm. Error bars represent ± s.e.m. $***P < 0.001$, one-way ANOVA.

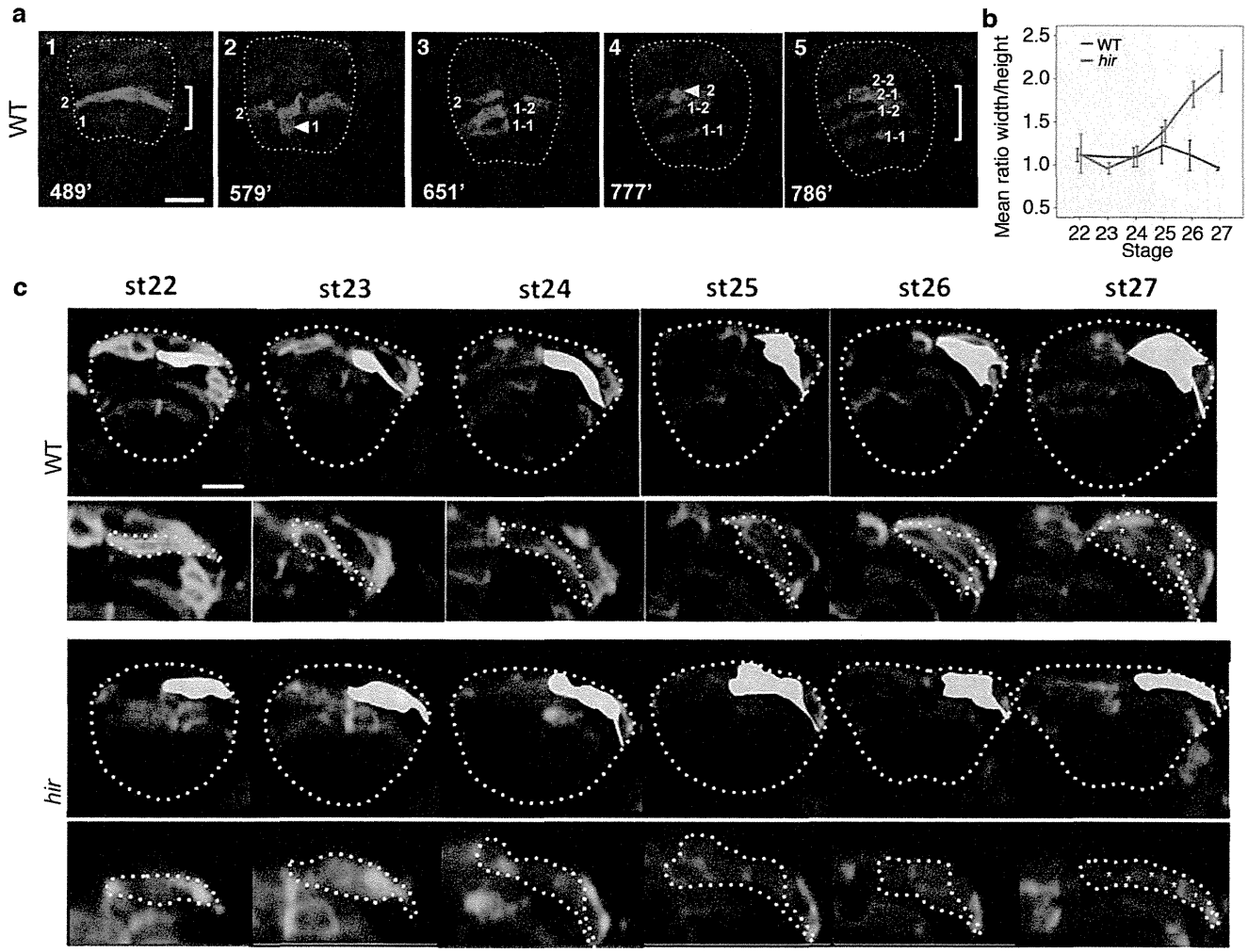

Extended Data Figure 4 | Flattening of the *hir* neural tube is associated with string-like cell arrangements. **a**, Increasing height (indicated by brackets in **a1** and **a5**) of WT neural tube (outlined, $n = 10$) was associated with cell stacking. Time in minutes from st. 21 shown bottom left of each sub-panel. Red fluorescent cells, for example, cell 1 in **a1**, labelled by photo-converting Kaede fluorescent protein, rounded up at the ventricular zone arrowhead in **a2** and divided along the ventricular zone (perpendicular cell division in **a3**) to generate stacked daughter cells 1-1, 1-2, making the neural tube thicker in **a5**. **b**, Width/height ratio of spinal cord, measured from time-lapse imaging of single embryos (WT, *hir* $n = 3$ each), showed that flattening occurred progressively in *hir*. Error bars are ± s.e.m. (see Source Data). **c**, Single-cell tracking of clones (labelled by membrane-GFP and nuclear-RFP) of the growing neural tube at the level of the fifth somite. Lower panels for WT and *hir* show magnified views of shaded regions in upper panels. The flatter and wider neural tube of the *hir* mutant at st. 27 was associated with long chain-like cell arrangements (asterisks, bottom panels of *hir*) tracked from a single neuroepithelial cell at st. 22, compared with the thick cell group generated by cell stacking in WT embryos. Scale bars, 40 μm.

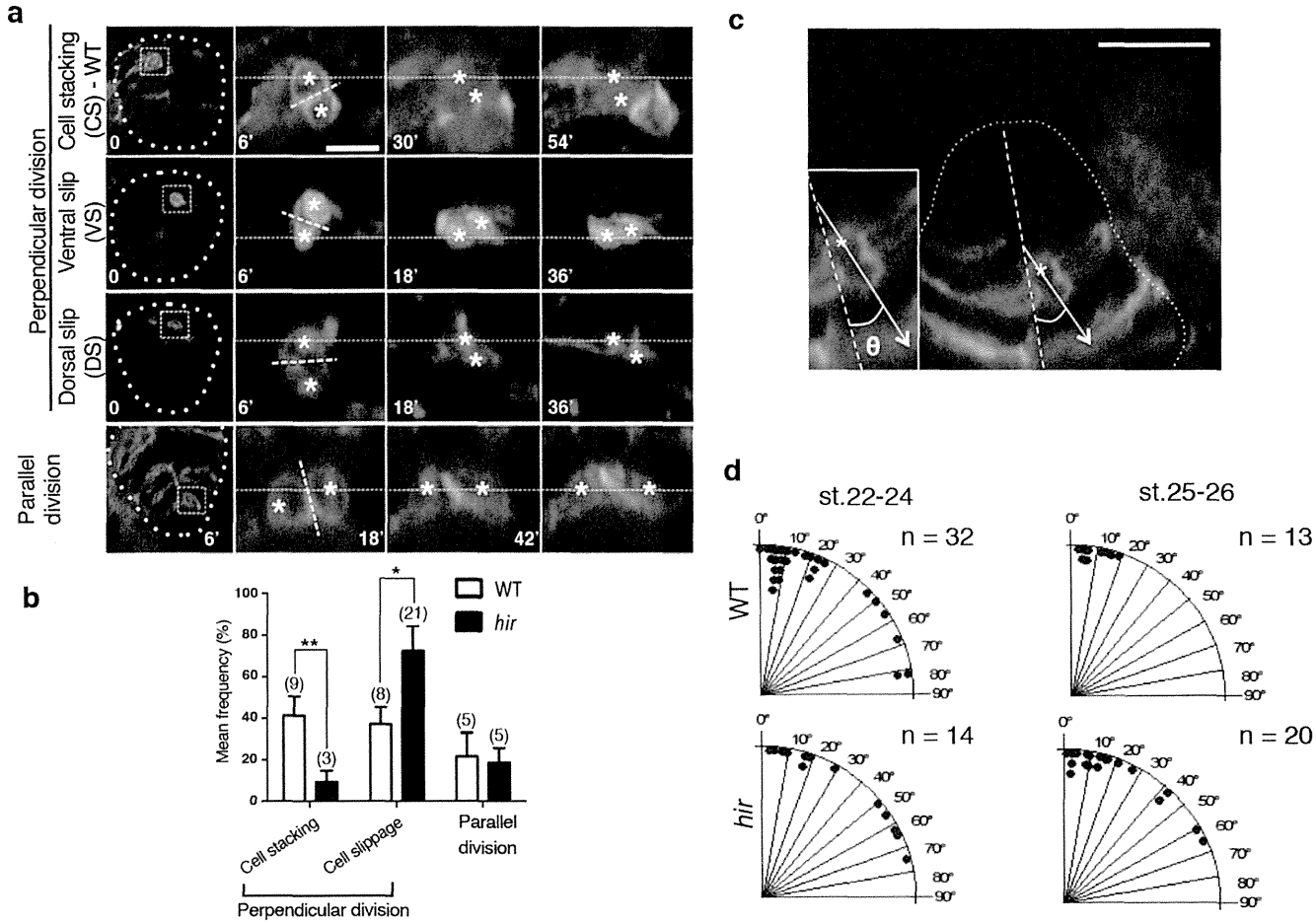

Extended Data Figure 5 | Flattening of the *hir* neural tube is associated with cell stacking failure. **a**–**d**, Single-cell analysis in *hir* neural tube shows cell stacking failure occurred after mitosis (**a**, **b**) and during mitosis (**c**, **d**). Neural progenitor cells divided with spindle orientation 'perpendicular' or 'parallel' to the ventricular zone ('perpendicular' or 'parallel' cell division, respectively). **a**, While daughter cells (asterisks) in WT remained stacked after 45 min following perpendicular cell division (first row), those in *hir* exhibited cell slippage (second and third rows). Telophase neuroepithelial cells in the neural tube, first column; magnified views in second to fourth columns. Dotted lines show division planes. Two types of cell slippage were observed: ventral slippage (VS) where the dorsal daughter cell slipped towards the ventral (second row), and dorsal slippage (DS) where the ventral daughter cell slipped towards the dorsal (third row). After parallel cell division, daughter cells did not change their positions in *hir* (fourth row). **b**, Cell stacking was reduced and cell slippage increased after perpendicular cell division, but cells after parallel cell division remained unaltered in *hir* mutants. Cell numbers in parentheses. Error bars, ± s.e.m. $*P < 0.05$, $**P < 0.01$, *t*-test (see Source Data). **c**, During perpendicular mitosis, daughter cells did not stack properly in *hir* mutants. Cell division orientation (*θ*) was measured in time-lapse sequences as the acute angle of the telophase cell axis against that of the ventricular zone (for example, dotted line 26° in **c**). **d**, Rose diagrams showing frequency and angle of parallel cell divisions. At st. 25–26 (50–54 hpf) perpendicular cell divisions generated stacked cells against gravitational forces in WT ($n = 3$ embryos at both stages). Far fewer stacked cells were observed in *hir* ($n = 4$ embryos at st. 22–24, $n = 3$ embryos at st. 25–26). These results are illustrated in Fig. 3a. Scale bars, 15 μm in **a**, 40 μm in **c**.

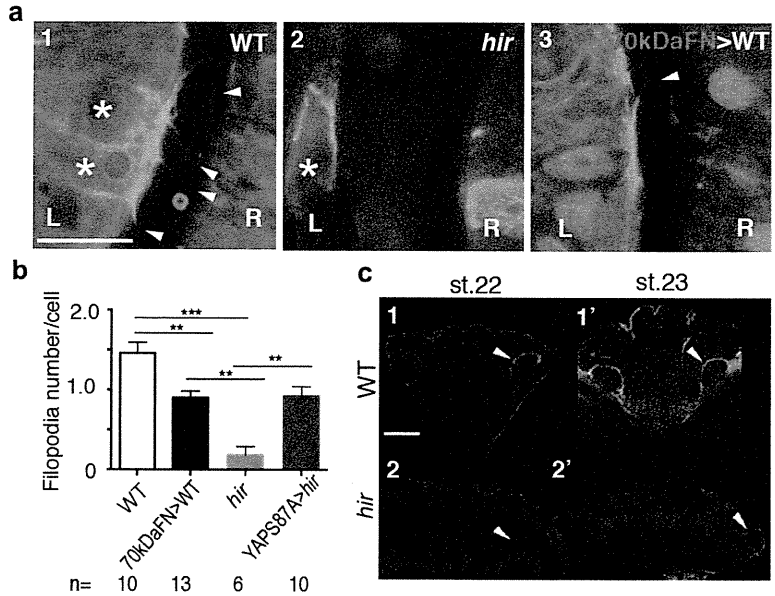

Extended Data Figure 6 | Detachment of lens is associated with loss of filopodia in *hir*. **a**, Representative live images of filopodia (arrowheads) from single lens cells (asterisks) expressing Lifeact–GFP in a mosaic manner; **a1**, WT; **a2**, *hir* and **a3**, 70kDaFN mRNA-injected WT embryos at st. 21.5 when lenses are detaching in *hir* mutants (see Extended Data Fig. 1b for larger views). **a3**, Non-mosaic expression of 70kDaFN mRNA in WT embryos was confirmed by co-injected H2A–red fluorescent protein (RFP) in the nucleus (red). L, lens; R, retina. **b**, Filopodia number per cell was determined (see Extended Data Fig. 7b4 for YAPS87A injected *hir* embryos). *n*, number of analysed embryos. Error bars indicate ± s.e.m. $^{**}P < 0.01$, $^{***}P < 0.001$, one-way ANOVA (Extended Data Fig. 6 Source Data). **c**, Transverse section of integrin-β1 IHC. Strong integrin-β1 localization between lens and retina in st. 22 WT ($n = 2$) (**c1**, arrowhead); no such localization in *hir* ($n = 3$) (**c2**). At st. 23 in *hir* ($n = 3$), weak localization where rounded up lens reattached to retina (**c2′**, arrowhead). Scale bars, 10 μm in **a**; 40 μm in **c**.

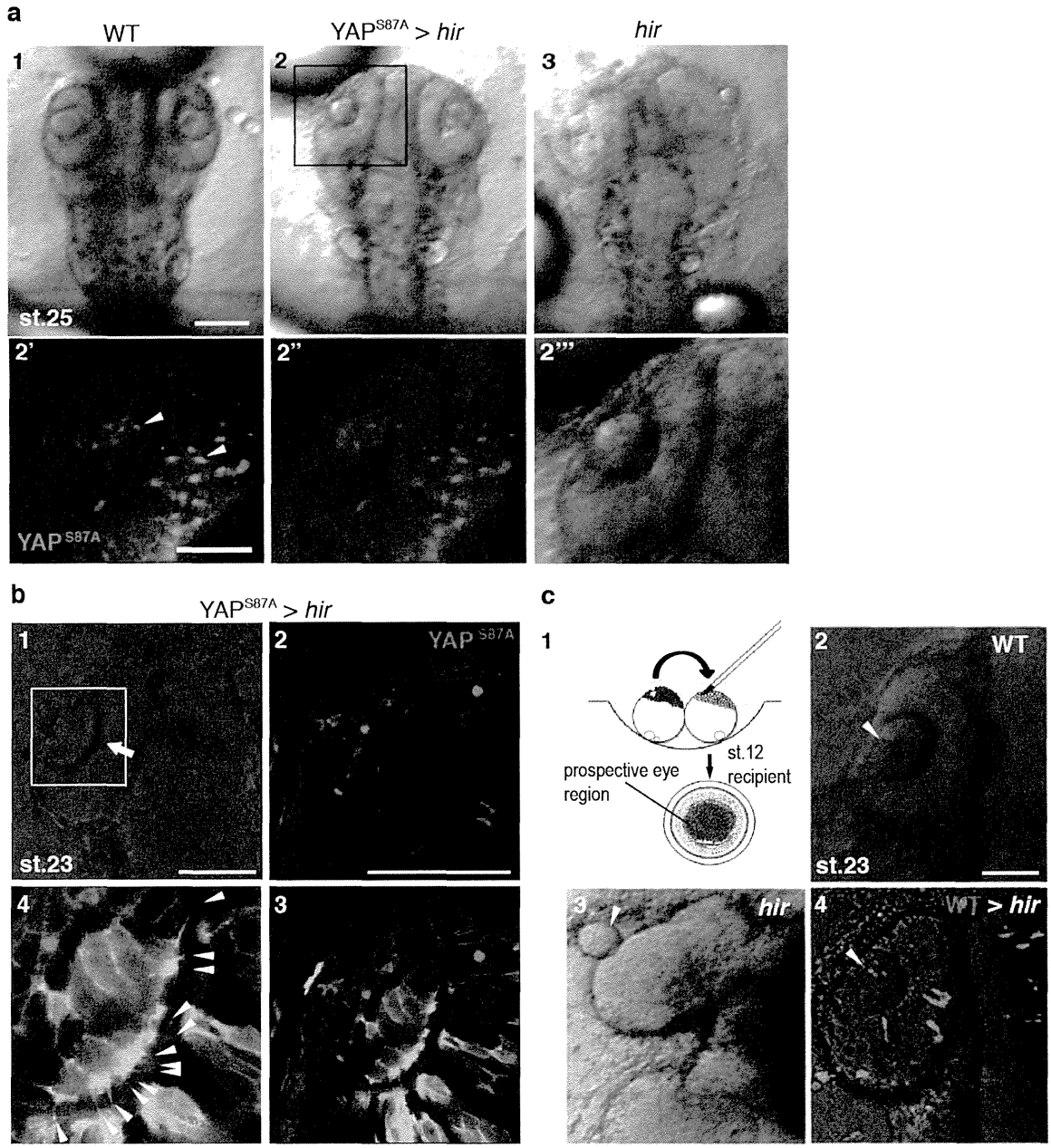

Extended Data Figure 7 | The *hir* mutation acts cell non-autonomously. **a**, Mosaic expression of EGFP–YAPS87A by mRNA injection at 16-cell stage in *hir* mutant embryos rescued the *hir* eye phenotype in a2 compared to a1 (WT) and a3 (*hir*). The boxed area in **a2** is magnified in the lower panels (**a2′**–**a2′′′**) fluorescence, merged and bright-field views, respectively. Arrowheads in **a2′** indicate EGFP–YAPS87A-expressing clones. **b**, Non-cell autonomous rescue of filopodia in *hir* mutant lens cells. YAPS87A+ mCherry-CAAX (labels membrane red) mRNA, and Lifeact-EGFP mRNA (labels F-actin green) were injected into different cells at 8–16 cell stage. **b1**, In the invaginated (arrow) *hir* mutant lens (boxed area magnified in **b2** and **b3**, $n = 10$) rescued by mosaic expression of YAPS87A (red), YAPS87A non-expressing mutant cells recovered filopodia (arrowheads in **b4**, magnified view of **b3**). Filopodia number/cell was compared between WT and *hir* in Extended Data Fig. 6b. **c1**, Cells from donor embryos injected with rhodamine (red, top left) were transplanted to a recipient embryo (top right, blastula stage st. 12) at the location fated to be eyes (bottom, animal pole view). **c2**, WT; **c3**, *hir* and **c4**, WT cells transplanted into *hir* mutant eye, causing the lens (arrowhead) to invaginate into the retina as in WT at st. 23 (note that this confocal sectional view represents a fraction of transplanted cells in the whole eye, see Supplementary Table 4 for the frequency of rescue). Scale bars, 40 μm.

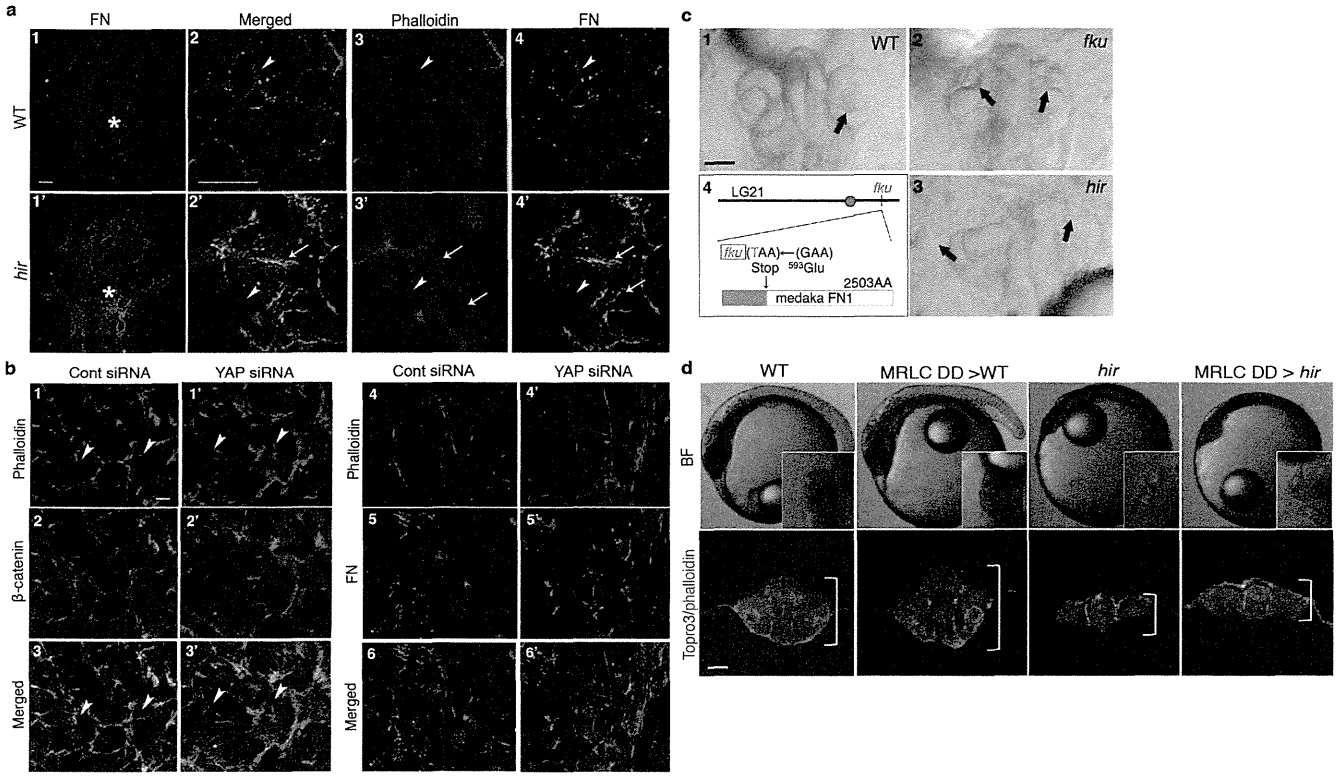

Extended Data Figure 8 | F-actin and FN localizations in *hir*. **a**, Whole-mount imaging of WT ($n = 5$) and *hir* ($n = 4$) embryos stained for F-actin (red) and FN (green). **a1**, **a1′**, Whole dorsal view of embryos anterior up, only FN shown; **a2**–**a4**, **a2′**–**a4′**, magnified view of area indicated by asterisks in **a1**, **a1′**; merged **a2**, **a2′**, F-actin **a3**, **a3′** and FN **a4**, **a4′**. Arrowheads indicate cortical F-actin and FN fibrils in WT and corresponding region in *hir* (**a3**, **a4**, **a3′**, **a4′**); arrows show ectopic F-actin aggregates and aberrant FN fibrils in **a3′**, **a4′**. **b**, Immunostaining of 2D cultured RPE1 cells transfected with control (Cont, $n = 21$) and YAP siRNAs ($n = 19$) stained with Phalloidin (**b1**, **b1′**), β-catenin (**b2**, **b2′**) and merged with DAPI (**b3**, **b3′**); phalloidin (**b4**, **4′**), FN (**b5**, **b5′**) and merged with DAPI (**b6**, **b6′**). In marked contrast to the 3D spheroids, FN deposits were not altered in YAP KD cells (**b5**, **b5′**) despite increased F-actin stress fibres (**b1**, **b1′** and **b4**, **b4′**). **c**, The medaka *fku* mutants exhibit lens dislocation (arrows). Live dorsal view of the head of **c1**, WT; **c2**, *fku* and **c3**, *hir* mutant embryos at st. 24. **c4**, The *fku* mutation was mapped to LG21 to the region encompassing the FN1 gene (0 recombinants/1,130 meiosis). Positional cloning identified a non-sense mutation of Glu593 (GAA to TAA) in FN1 (2,503 amino acids). FN1 morpholino KD in WT embryos mimicked the *fku* mutant phenotype. **d**, Constitutive-active MRLC-DD mRNA markedly increased body thickness of WT embryos, but did not rescue the flattened body (brackets in lower panels) and dislocated lens phenotypes of *hir* ($n = 48$). Upper panels, live lateral view (insets, dorsal views of left eyes); lower panels, frontal sections stained with phalloidin (red) and TO-PRO-3 (blue) at st. 25. Scale bars 30 μm, except **a2**, 15 μm and **b1**, 50 μm.

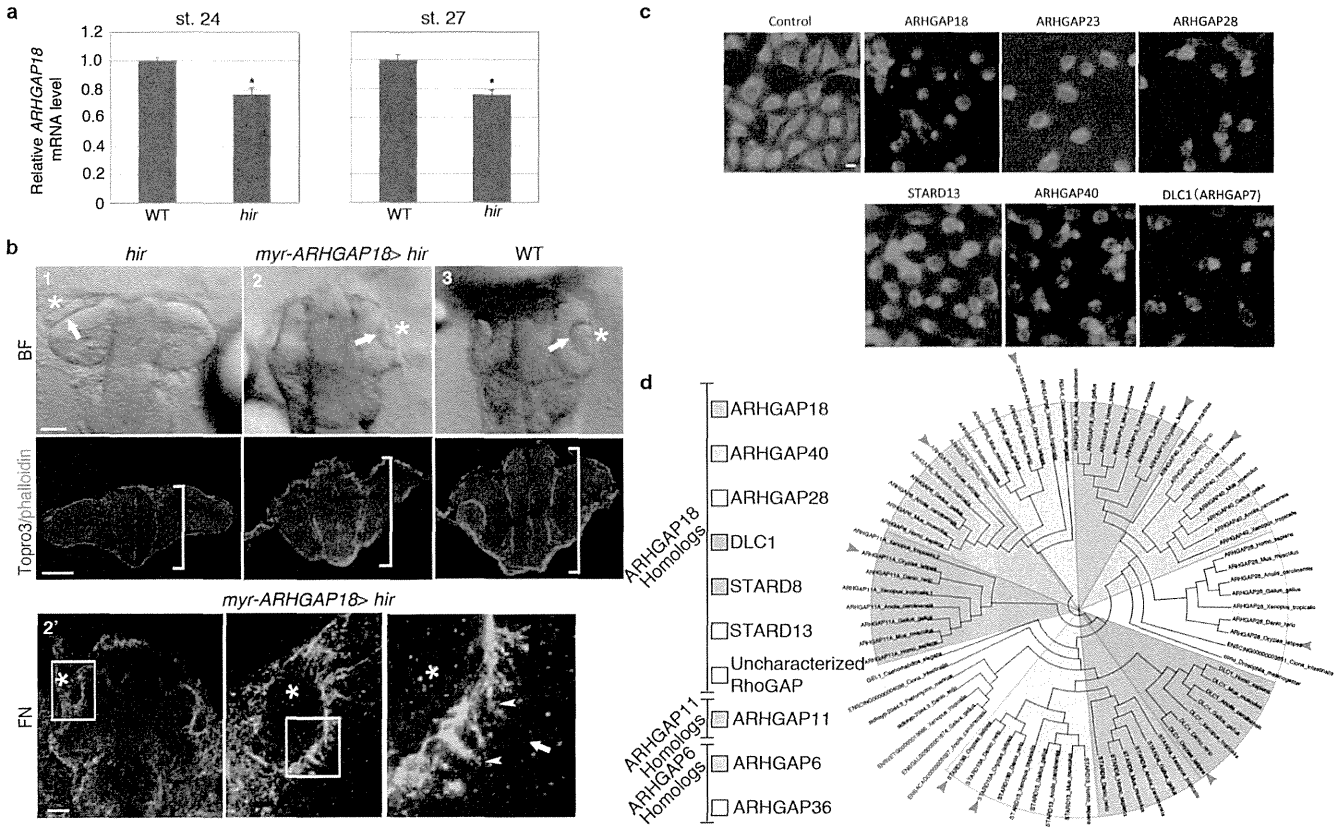

Extended Data Figure 9 | *in vivo* analysis of ARHGAP18 function. **a**, Quantitative RT–PCR analysis showed that *ARHGAP18* mRNA expression in the *hir* mutant is significantly reduced to 76% of WT level. EF1α used as an internal control. Data are shown as means ± s.e.m. ($n = 10$ each; $^*P < 0.001$ Student's *t*-test (two-tailed)). **b**, *myrARHGAP18* mRNA (150 pg) injection rescued the *hir* phenotype (21 rescued/39 *hir*/112 survived embryos). Upper panels, live dorsal view; lower panels, frontal sections stained with phalloidin (red) and TO-PRO-3 (blue) at st. 23; **b1**, uninjected *hir*, **b2**, injected *hir* and **b3**, WT. The lens (asterisk) invaginated into retina (arrows, upper panel) and the neural tube became thicker (brackets in lower panels) in the *myrARHGAP18* mRNA-injected *hir* mutant embryos. **b2′**, FN staining of *myrARHGAP18* mRNA-injected *hir* mutant embryos; boxed area magnified in subsequent panel to the right; invaginated lenses had fine FN fibrils (arrowheads) between lens and retina as in WT (see Fig. 3b1′′). **c**, Phylogenetic analysis identified 16 ARHGAP18 paralogues in vertebrate lineages. Arrowheads show medaka orthologues. **d**, siRNA screening of 40 human ARHGAP genes in HeLa cells showed that KD of five ARHGAP genes exhibited the rounding up phenotype similar to ARHGAP18 inactivation. Scale bars, 30 μm.

nature COMMUNICATIONS

ARTICLE

Received 3 Jun 2014 | Accepted 13 Aug 2014 | Published 19 Sep 2014

DOI: 10.1038/ncomms5982

Macrophage-inducible C-type lectin underlies obesity-induced adipose tissue fibrosis

Miyako Tanaka[1,*], Kenji Ikeda[1,*], Takayoshi Suganami[2,3], Chikara Komiya[1], Kozue Ochi[1], Ibuki Shirakawa[2], Miho Hamaguchi[1], Satoshi Nishimura[4,5,6], Ichiro Manabe[4], Takahisa Matsuda[7], Kumi Kimura[8], Hiroshi Inoue[8], Yutaka Inagaki[9], Seiichiro Aoe[10], Sho Yamasaki[11] & Yoshihiro Ogawa[1]

In obesity, a paracrine loop between adipocytes and macrophages augments chronic inflammation of adipose tissue, thereby inducing systemic insulin resistance and ectopic lipid accumulation. Obese adipose tissue contains a unique histological structure termed crown-like structure (CLS), where adipocyte-macrophage crosstalk is known to occur in close proximity. Here we show that Macrophage-inducible C-type lectin (Mincle), a pathogen sensor for *Mycobacterium tuberculosis*, is localized to macrophages in CLS, the number of which correlates with the extent of interstitial fibrosis. Mincle induces obesity-induced adipose tissue fibrosis, thereby leading to steatosis and insulin resistance in liver. We further show that Mincle in macrophages is crucial for CLS formation, expression of fibrosis-related genes and myofibroblast activation. This study indicates that Mincle, when activated by an endogenous ligand released from dying adipocytes, is involved in adipose tissue remodelling, thereby suggesting that sustained interactions between adipocytes and macrophages within CLS could be a therapeutic target for obesity-induced ectopic lipid accumulation.

[1] Department of Molecular Endocrinology and Metabolism, Graduate School of Medical and Dental Sciences, Tokyo Medical and Dental University, Tokyo 113-8510, Japan. [2] Department of Organ Network and Metabolism, Graduate School of Medical and Dental Sciences, Tokyo Medical and Dental University, Tokyo 113-8510, Japan. [3] Japan Science and Technology Agency, PRESTO, Tokyo, Japan. [4] Department of Cardiovascular Medicine, The University of Tokyo, Tokyo 113-8655, Japan. [5] Translational Systems Biology and Medicine Initiative, The University of Tokyo, Tokyo 113-8655, Japan. [6] Jichi Medical University, Tochigi 329-0498, Japan. [7] Pharmaceutical Research Division, Takeda Pharmaceutical Company, Fujisawa 251-8555, Japan. [8] Department of Physiology and Metabolism, Brain/Liver Interface Medicine Research Center, Kanazawa University, Kanazawa 920-8641, Japan. [9] Department of Regenerative Medicine, Center for Matrix Biology and Medicine, Tokai University School of Medicine, Isehara 259-1193, Japan. [10] Department of Home Economics, Otsuma Women's University, Tokyo 102-8357, Japan. [11] Division of Molecular Immunology, Medical Institute of Bioregulation, Kyushu University, Fukuoka 812-8582, Japan. * These authors contributed equally to this work. Correspondence and requests for materials should be addressed to T.S. (email: suganami.mem@tmd.ac.jp) or to Y.O. (email: ogawa.mem@tmd.ac.jp).

Obesity is a state of chronic, low-grade inflammation[1,2]. Indeed, adipose tissue in obesity is characterized by adipocyte hypertrophy, followed by increased angiogenesis, immune cell infiltration, extracellular matrix overproduction, which is referred to as 'adipose tissue remodelling'[3,4]. As a molecular mechanism, we have provided evidence that a paracrine loop involving saturated fatty acids and tumour necrosis factor-α (TNFα) derived from adipocytes and macrophages, respectively, establishes a vicious cycle, thereby accelerating the inflammatory change in obese adipose tissue[5]. It is conceivable that increased adipose tissue inflammation stimulates adipocyte lipolysis and tissue fibrosis, and thus enhances the release of free fatty acids from the adipose tissue, which may be accumulated in non-adipose tissue such as liver and skeletal muscle, as ectopic fat, and induce a variety of metabolic abnormalities called lipotoxicity[3,4]. In this regard, Khan *et al.*[6] reported that mice lacking collagen VI, which is expressed abundantly in adipose tissue, exhibit the uninhibited adipose tissue expansion and substantial improvement in insulin sensitivity on a high-fat diet (HFD). Although recent evidence suggests a role for obesity-induced hypoxic state[7,8], the molecular mechanisms underlying adipose tissue fibrosis are still largely unknown.

As the site of crosstalk between adipocytes and macrophages, there is a unique structure in obese adipose tissue called crown-like structure (CLS), where macrophages are considered to scavenge the residual lipid droplets of dead adipocytes[9,10]. Histologically, proinflammatory M1 macrophages aggregate to constitute CLS in obese adipose tissue of humans and rodents. On the other hand, M2 macrophages are scattered in the interstitial spaces between adipocytes[10]. Notably, the number of CLS is positively correlated with systemic insulin resistance in obese subjects[11,12], suggesting the pathophysiologic role of CLS in adipose tissue inflammation and systemic energy metabolism. However, how CLS is formed in adipose tissue during the course of obesity and how it is involved in adipose tissue remodelling are poorly understood.

Macrophage-inducible C-type lectin (Mincle, Clec4e or Clecsf9) is a pathogen sensor that recognizes pathogenic fungi and *Mycobacterium tuberculosis*[13–16], and as the name implies, it is induced in macrophages by lipopolysaccharide through Toll-like receptor 4 (TLR4; ref. 17). We previously reported that saturated fatty acids also induce *Mincle* expression in macrophages through TLR4 (ref. 18). Moreover, the obesity-induced increase in *Mincle* expression in adipose tissue is markedly attenuated in C3H/HeJ mice with defective TLR4 signalling relative to control C3H/HeN mice[18]. Yamasaki *et al.* reported that Mincle can sense cell death as well to induce proinflammatory cytokine production and suggested the role of Mincle in sterile inflammation[19]. We have recently demonstrated that *Mincle* is induced in adipose tissue macrophages during the interaction between adipocytes and macrophages, at least partly, through the saturated fatty acid/TLR4/NF-κB pathway[18]. It is currently unclear whether Mincle regulates adipose tissue inflammation and thus systemic energy metabolism in obesity, and if so, how it does remains to be elucidated.

Here we show that *Mincle*, when induced during the development of obesity, is localized to macrophages constituting CLS in adipose tissue. Interestingly, *Mincle* KO mice are protected against obesity-induced CLS formation and adipose tissue fibrosis, followed by reduced ectopic lipid accumulation and insulin resistance in the liver. On the other hand, treatment with trehalose-6,6′-dimycolate (TDM), a mycobacterial cell wall glycolipid that is known to be a Mincle ligand[13], induces CLS formation and interstitial fibrosis in adipose tissue in mice. Mincle stimulation also induces potently expression of fibrosis-related genes in macrophages *in vitro*. This study provides evidence that Mincle has a role in the crosstalk between adipocytes and macrophages in CLS, thereby leading to activation of fibrogenic programme. Our data also suggest that antagonism of Mincle in macrophages offers a novel therapeutic strategy to prevent or treat obesity-induced adipose tissue fibrosis and thus ectopic lipid accumulation.

Results

Adipose tissue *Mincle* expression in obesity. We previously reported that *Mincle* expression is markedly upregulated in adipose tissue macrophages in obesity[18]. In this study, we first examined the time course of *Mincle* mRNA expression in epididymal fat tissue of wild-type mice fed a HFD and found that *Mincle* mRNA expression was roughly constant in wild-type mice fed a standard diet (SD) throughout the experimental period. On the other hand, *Mincle* mRNA expression was significantly increased in wild-type mice fed a HFD relative to those fed a SD at 16 weeks and gradually increased up to 50 weeks. There was no significant difference in expression of *Emr1*, which encodes macrophage marker F4/80, between 16 and 50 weeks (Fig. 1a). *Mincle* mRNA expression was also increased in liver to a lesser extent than epididymal fat tissue (Fig. 1b). At 16 weeks, *Mincle* mRNA expression was markedly high in epididymal fat tissue relative to subcutaneous fat tissue, which was roughly in parallel with *Emr1* mRNA expression (Fig. 1c). In the stromal-vascular fraction (SVF) from epididymal fat tissue of genetically obese *ob/ob* mice, *Mincle* mRNA was exclusively expressed in $CD45^+CD11b^+F4/80^+$ cells or macrophages (Fig. 1d). In line with this, flow cytometric analysis revealed that obesity markedly increased the number of Mincle-positive macrophages, whereas there was no appreciable Mincle expression in other immune cells (Fig. 1e).

Altered lipid distribution in *Mincle* KO mice. We next examined the metabolic phenotypes of *Mincle* KO mice at 16 weeks of HFD feeding. There was no appreciable difference in body weight and subcutaneous fat weight between the genotypes (Fig. 2a and Supplementary Fig. 1a). The epididymal fat weight was significantly increased with reciprocal reduction of the liver weight in *Mincle* KO mice relative to wild-type mice on a HFD (Fig. 2a and Supplementary Fig. 1a). Histological examination revealed that hepatic steatosis was markedly attenuated in *Mincle* KO mice relative to wild-type mice (Fig. 2b). Consistently, hepatic triglyceride content and serum free fatty acid (FFA) and alanine aminotransferase (ALT) concentrations were significantly reduced in *Mincle* KO mice relative to wild-type mice (Fig. 2c,d). Basically, similar results were obtained in *Mincle* KO mice fed a HFD for 50 weeks (Supplementary Fig. 2a,b). On the other hand, at 8 weeks of HFD feeding when there was no apparent difference in *Mincle* expression in epididymal fat tissue between the diets (Fig. 1a), we did not observe any difference in the body weight and tissue weights between the genotypes (Supplementary Fig. 3). These observations suggest the altered lipid distribution in adipose tissue and liver in *Mincle* KO mice on a HFD.

Ameliorated glucose metabolism in *Mincle* KO mice. We performed the glucose tolerance test at 16 weeks of HFD feeding and found that *Mincle* KO mice showed better glucose tolerance and lower serum insulin concentrations than wild-type mice (Supplementary Fig. 1b). Moreover, the insulin-induced phosphorylation of Akt was significantly increased in the liver of *Mincle* KO mice relative to that of wild-type mice (Supplementary Fig. 1c). The phosphorylated Akt levels also tended to increase in the adipose tissue and skeletal muscle in *Mincle* KO mice, which

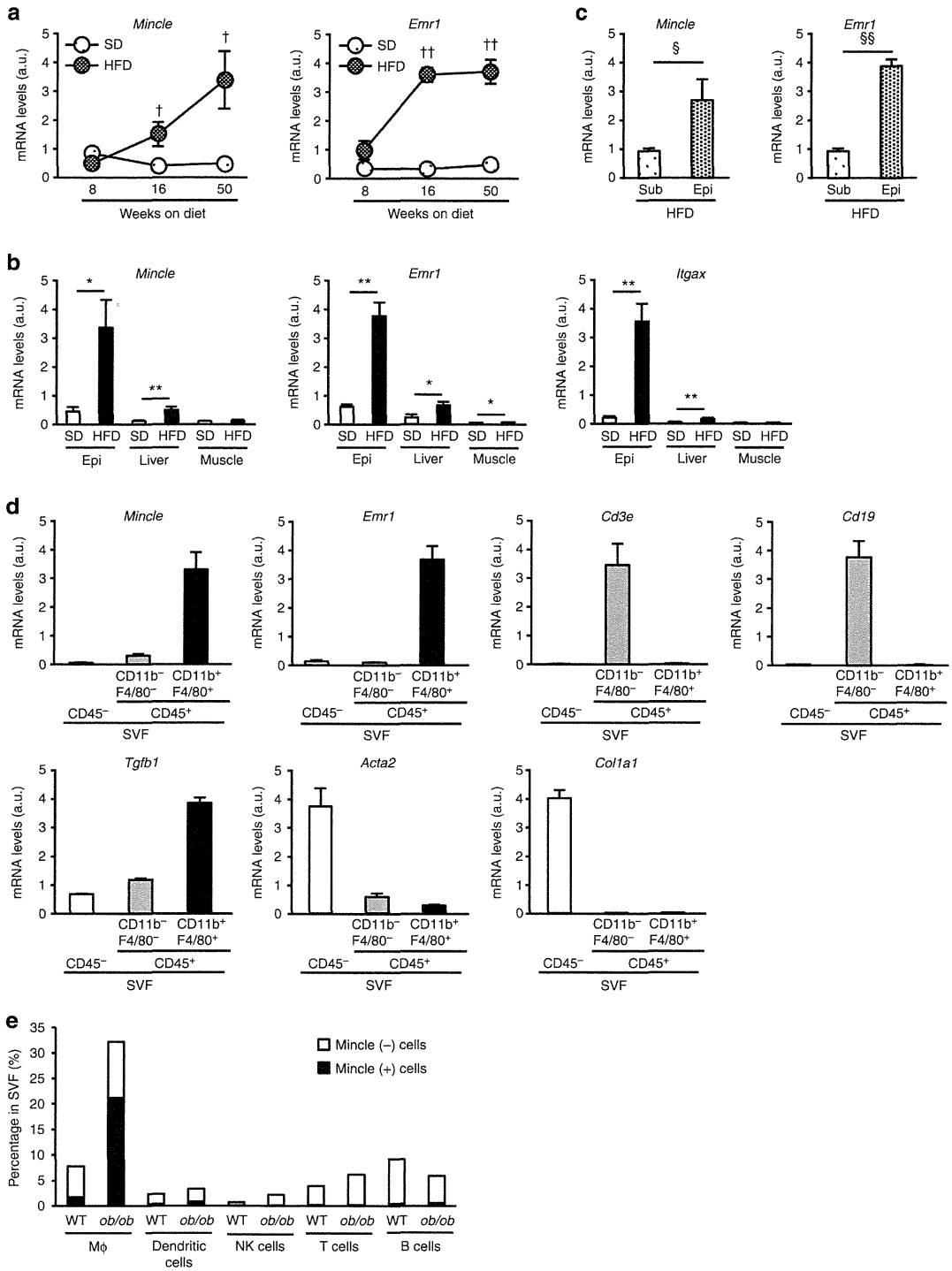

Figure 1 | Adipose tissue *Mincle* expression and Mincle-expressing cells in obese adipose tissue. (**a**) Time course of *Mincle* mRNA and *Emr1* (F4/80) expression in epididymal fat tissue of wild-type mice fed a HFD or a SD for up to 50 weeks. Values are mean ± s.e.m. The data are analysed by unpaired *t*-test; $n=5$ to 11; $^{\dagger}P<0.05$, $^{\dagger\dagger}P<0.01$ versus SD at each time point. (**b**) mRNA expression of *Mincle*, *Emr1* and *Itgax* (CD11c) in epididymal fat tissue (Epi), liver and skeletal muscle in wild-type mice fed a HFD for 50 weeks. Values are mean ± s.e.m. The data are analysed by unpaired *t*-test; $n=5$ to 10; $^{*}P<0.05$, $^{**}P<0.01$. (**c**) *Mincle* mRNA expression in epididymal (Epi) and subcutaneous (Sub) fat tissues of wild-type mice on a HFD for 16 weeks. Values are mean ± s.e.m. The data are analysed by unpaired *t*-test; $n=11$; $^{\S}P<0.05$, $^{\S\S}P<0.01$. (**d**) mRNA expression of *Mincle*, *Emr1*, *Acta2* (αSMA), and other cell type markers in $CD45^-$, $CD45^+CD11b^-F4/80^-$ and $CD45^+CD11b^+F4/80^+$ cells isolated from SVF. Values are mean ± s.e.m.; $n=4$. (**e**) Percentage of Mincle-expressing cells in various immune cells in SVF. Values are the average of four samples.

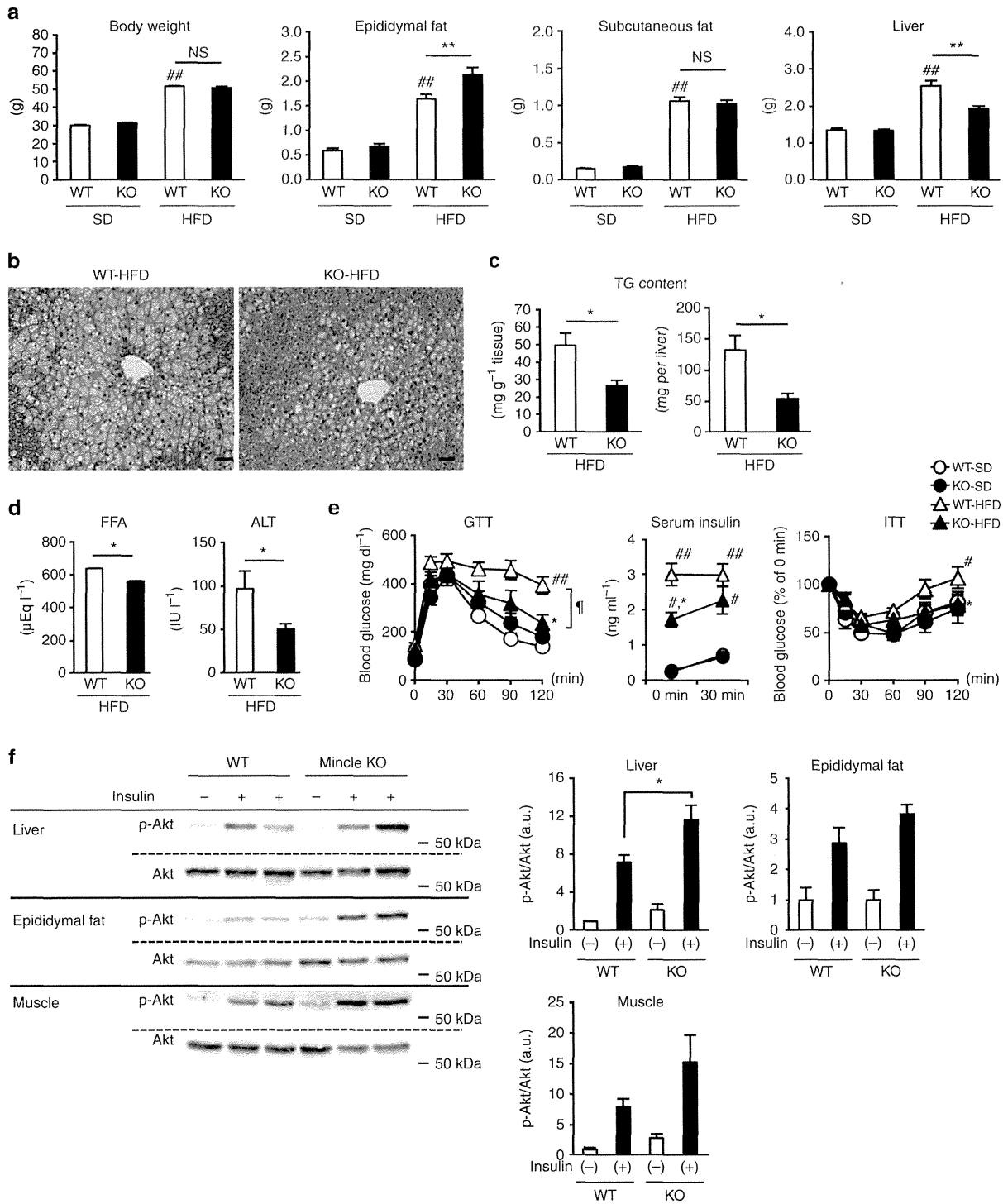

Figure 2 | Altered lipid distribution between adipose tissue and liver in *Mincle* KO mice. (**a**) Body weight and fat and liver weights of *Mincle* KO and wild-type mice at 16 weeks. Values are mean ± s.e.m. The data are analysed by analysis of variance (ANOVA) followed by Tukey–Kramer test. $^{\#\#}P<0.01$ versus WT-SD, $^{**}P<0.01$. NS, not significant; $n=11$ to 13. (**b**–**d**) Representative hematoxylin and eosin staining of the liver (**b**), hepatic triglyceride (TG) content (**c**) and serum FFA and ALT concentrations (**d**) in *Mincle* KO and wild-type mice at 16 weeks. Original magnification, ×200; Scale bar, 50 μm. Values are mean ± s.e.m. The data are analysed by unpaired *t*-test. $^{*}P<0.05$; $n=11$ to 13. (**e**,**f**) Glucose metabolism in *Mincle* KO and wild-type mice fed a HFD for 50 weeks; $n=5$ to 8. (**e**) Glucose and insulin tolerance tests. Values are mean ± s.e.m. The data are analysed by ANOVA followed by Tukey–Kramer test. $^{\#}P<0.05$, $^{\#\#}P<0.01$ versus WT-SD and $^{*}P<0.05$ versus WT-HFD at each point. $^{\P}P<0.05$ assessed by ANOVA with repeated-measures analysis. (**f**) Western blotting of phosphorylated Akt (Thr308) in liver, epididymal fat tissue and soleus muscle. Values are mean ± s.e.m. The data are analyzed by ANOVA followed by Tukey–Kramer test; $^{*}P<0.05$.

did not reach statistical significance. In addition, there was a slight decrease in the insulin-positive area and the number of Ki67-positive cells in the pancreas of *Mincle* KO mice relative to that of wild-type mice, whereas the islet area and glucagon-positive area did not differ between the genotypes (Supplementary Fig. 4). These observations suggest that reduced insulin resistance in the liver leads to better glucose tolerance in *Mincle* KO mice. We confirmed similar results at 50 weeks (Fig. 2e,f and Supplementary Fig. 2c). Collectively, HFD-induced insulin resistance was ameliorated in the liver of *Mincle* KO mice along with reduced hepatic lipid accumulation.

Reduced adipose tissue fibrosis in *Mincle* KO mice. Histological analysis of epididymal fat tissue revealed that adipocyte cell size appears to be increased in *Mincle* KO mice relative to wild-type mice on a HFD for 16 weeks, whereas there was no significant difference in the number of adipocytes (Fig. 3a). In this study, mRNA expression of genes related to adipogenesis, lipogenesis, lipolysis and β-oxidation did not differ between the genotypes (Supplementary Fig. 5). In addition, flow cytometric analysis showed no significant difference in the ratio of each immune cell to the SVF (Supplementary Fig. 6). On the other hand, Masson's trichrome staining revealed extensive interstitial fibrosis in epididymal fat tissue of wild-type mice, which is markedly suppressed in *Mincle* KO mice (Fig. 3b,c). We also obtained similar results by Sirius red staining and measurement of total collagen content (Fig. 3d–f). Consistently, there was a significant decrease in the area of αSMA-positive cells or myofibroblasts in *Mincle* KO mice relative to wild-type mice (Fig. 3g,h). Interestingly, there was no significant difference in total collagen content of subcutaneous fat tissue between the genotypes (Fig. 3f). We confirmed these results in *Mincle* KO mice fed a HFD for 50 weeks (Supplementary Fig. 2d,e). Collectively, these observations indicate reduced interstitial fibrosis in epididymal fat tissue of *Mincle* KO mice relative to wild-type mice.

Since Mincle is expressed selectively in adipose tissue macrophages (Fig. 1e), we next performed bone marrow transplantation (BMT) experiments to confirm the role of Mincle in bone marrow-derived cells. In this study, the substitution rate of BMT was more than 90% (Supplementary Fig. 7a). *Mincle* mRNA expression in epididymal fat tissue was almost negligible in bone marrow-specific *Mincle* KO mice (Mincle KO-BM mice) compared with the control mice (EGFP-BM mice) (Supplementary Fig. 7b), suggesting the macrophage-selective expression of Mincle (Fig. 1d). Under these experimental conditions, we confirmed that *Mincle* deficiency protected against HFD-induced adipose tissue fibrosis (Supplementary Fig. 7c).

Reduced CLS formation in adipose tissue of *Mincle* KO mice. To determine the localization of *Mincle* expression in obese adipose tissue, we performed *in situ* hybridization analysis and found that *Mincle* occurs in some of the macrophages constituting CLS in epididymal fat tissue (Fig. 4a,b). Flow cytometric analysis revealed that $CD11b^+F4/80^{lo}$ cells isolated from the SVF showed higher *Mincle* mRNA expression than $CD11b^+F4/80^{hi}$ cells (Fig. 4c). $CD11b^+F4/80^{lo}$ cells expressed higher *Itgax* (CD11c) and lower *Mrc1* (CD206) mRNA levels than $CD11b^+F4/80^{hi}$ cells. These observations are consistent with our previous data that *Mincle* is expressed selectively in proinflammatory M1 macrophages *in vitro*[18]. Interestingly, the CLS density in *Mincle* KO mice was markedly reduced relative to wild-type mice (Fig. 4d,e). Moreover, there was a significant decrease in *Tnfa* (TNFα) mRNA expression in *Mincle* KO mice relative to wild-type mice on a HFD (Fig. 4f). On the other hand, there was no significant difference in macrophage number (Fig. 4e) and polarization (Fig. 4f and Supplementary Fig. 6b) between the genotypes. By double-immunofluorescent staining of F4/80 (green) and collagen I (red), we observed the adjacent spatial relationship between CLS and fibrotic regions (Fig. 4g). The CLS density was positively correlated with the extent of adipose tissue fibrosis determined by Masson's trichrome and Sirius red stainings (Fig. 4h). Collectively, these observations suggest that Mincle-mediated CLS formation has a role in interstitial fibrosis in adipose tissue.

Mincle-stimulated fibrogenic gene expression in macrophages. To elucidate how Mincle regulates adipose tissue fibrosis, we performed DNA microarray analysis of peritoneal macrophages stimulated with TDM (Fig. 5a). A total of 179 genes were upregulated by TDM in wild-type macrophages and the effect was totally abolished in *Mincle* KO macrophages (Supplementary Table 1), indicating the Mincle-specific activation by TDM. In addition to known chemokine and cytokine genes, pathway analysis using Reactome database (http://www.reactome.org/) identified several large clusters related to tissue remodelling (Supplementary Fig. 8). By quantitative real-time PCR, we confirmed that TDM treatment markedly increases mRNA expression of *Tgfb1* (TGFβ1), *Pdgfb* and *Timp1* (Fig. 5b), which regulate extracellular matrix (ECM) production, fibroblast proliferation and ECM degradation, respectively[20]. Since the Fc receptor common γ-chain (FcRγ)-spleen tyrosine kinase (Syk) cascade is shown to be downstream of Mincle signalling[19], we examined the involvement of Syk in the induction of fibrosis-related genes. Treatment with a Syk-inhibitor suppressed dose-dependently the mRNA expression of *Tgfb1*, *Pdgfb* and *Timp1* along with *Cxcl2* (MIP-2), a chemokine that is induced by the Mincle-Syk pathway[19] (Fig. 5c). These observations suggest that Mincle activation potently induces fibrosis-related genes through Syk in macrophages.

Mincle-stimulated increase of myofibroblasts in SVF. Since activated fibroblasts or myofibroblasts are crucial for fibrogenesis in various tissues and organs[20,21], we next examined the effect of Mincle stimulation of SVF that contains a variety of cell types such as immune cells, vascular cells and fibroblasts (Fig. 6a). The SVF was prepared from epididymal fat tissue of 9-week-old *ob/ob* mice; they showed high macrophage infiltration and *Mincle* expression relative to wild-type mice as reported[18]. Stimulation with TDM for 1 day significantly increased *Mincle*, *Tnfa*, *Pdgfb* and *Timp1* mRNA expression in the SVF (Fig. 6b). The effect of Mincle stimulation was also observed after 3 days (Fig. 6b). Interestingly, mRNA expression of *Acta2*, which encodes the myofibroblast marker αSMA, was significantly increased by Mincle stimulation (Fig. 6b). To address the effect of Mincle activation in macrophages on adipose tissue fibroblasts, we co-cultured peritoneal macrophages with $CD45^-CD31^-$ cells prepared from the SVF of *ob/ob* mice which should abundantly include fibroblasts (Fig. 6c). Stimulation of the co-culture with TDM time-dependently increased mRNA expression of *Acta2*, which was followed by the increase of *Col1a1* (collagen I) mRNA expression (Fig. 6d). These observations strongly suggest that Mincle activation in macrophages effectively increases the number of myofibroblasts in adipose tissue.

Mincle-stimulated interstitial fibrosis in adipose tissue. We next examined whether stimulation of Mincle is sufficient to induce interstitial fibrosis in adipose tissue *in vivo*. Emulsion containing TDM or vehicle was injected directly into epididymal